

# A disordered rock salt anode for fast-charging lithium-ion batteries

<https://doi.org/10.1038/s41586-020-2637-6>

Received: 16 December 2019

Accepted: 8 July 2020

Published online: 2 September 2020

 Check for updates

Haodong Liu<sup>1,13</sup>, Zhuoying Zhu<sup>1,13</sup>, Qizhang Yan<sup>1</sup>, Sicen Yu<sup>1</sup>, Xin He<sup>2</sup>, Yan Chen<sup>3</sup>, Rui Zhang<sup>4</sup>, Lu Ma<sup>5</sup>, Tongchao Liu<sup>6</sup>, Matthew Li<sup>6</sup>, Ruqian Lin<sup>7</sup>, Yiming Chen<sup>1</sup>, Yejing Li<sup>1</sup>, Xing Xing<sup>1</sup>, Yoonjung Choi<sup>1</sup>, Lucy Gao<sup>8</sup>, Helen Sung-yun Cho<sup>9</sup>, Ke An<sup>3</sup>, Jun Feng<sup>10</sup>, Robert Kostecki<sup>2</sup>, Khalil Amine<sup>6</sup>, Tianpin Wu<sup>11</sup>, Jun Lu<sup>6,✉</sup>, Huolin L. Xin<sup>4,✉</sup>, Shyue Ping Ong<sup>1,12,✉</sup> & Ping Liu<sup>1,12,✉</sup>

Rechargeable lithium-ion batteries with high energy density that can be safely charged and discharged at high rates are desirable for electrified transportation and other applications<sup>1–3</sup>. However, the sub-optimal intercalation potentials of current anodes result in a trade-off between energy density, power and safety. Here we report that disordered rock salt<sup>4,5</sup>  $\text{Li}_{3+x}\text{V}_2\text{O}_5$  can be used as a fast-charging anode that can reversibly cycle two lithium ions at an average voltage of about 0.6 volts versus a  $\text{Li}/\text{Li}^+$  reference electrode. The increased potential compared to graphite<sup>6,7</sup> reduces the likelihood of lithium metal plating if proper charging controls are used, alleviating a major safety concern (short-circuiting related to Li dendrite growth). In addition, a lithium-ion battery with a disordered rock salt  $\text{Li}_3\text{V}_2\text{O}_5$  anode yields a cell voltage much higher than does a battery using a commercial fast-charging lithium titanate anode or other intercalation anode candidates ( $\text{Li}_3\text{VO}_4$  and  $\text{LiV}_{0.5}\text{Ti}_{0.5}\text{S}_2$ )<sup>8,9</sup>. Further, disordered rock salt  $\text{Li}_3\text{V}_2\text{O}_5$  can perform over 1,000 charge–discharge cycles with negligible capacity decay and exhibits exceptional rate capability, delivering over 40 per cent of its capacity in 20 seconds. We attribute the low voltage and high rate capability of disordered rock salt  $\text{Li}_3\text{V}_2\text{O}_5$  to a redistributive lithium intercalation mechanism with low energy barriers revealed via ab initio calculations. This low-potential, high-rate intercalation reaction can be used to identify other metal oxide anodes for fast-charging, long-life lithium-ion batteries.

Lithium-rich disordered rock salt (DRS) oxides are known to be promising cathode materials, with fast lithium (Li) diffusion that is due to a percolating network of octahedron–tetrahedron–octahedron pathways<sup>4,10</sup>. However, although the formation of DRS such as  $\text{Li}_3\text{MoO}_4$  and  $\text{Li}_3\text{W}_2\text{O}_7$  oxides during electrochemical reactions is known<sup>11,12</sup>, there have been no investigations of further insertion of Li into DRS oxides to form potential anode materials. Delmas showed that three Li ions could intercalate into  $\text{V}_2\text{O}_5$  to form  $\text{Li}_3\text{V}_2\text{O}_5$  when the discharge cut-off voltage is extended to 1.9 V, with the proposed structure to be a rock salt phase with crystallographic formula  $\text{Li}_{0.6}\text{V}_{0.4}\text{O}$  (refs. <sup>13,14</sup>). Extended Data Fig. 1a, b presents the voltage curve and phase transformations of  $\text{V}_2\text{O}_5$  during its first lithiation down to 0.01 V. The results at above 1.5 V are consistent with previous reports<sup>13</sup>. Surprisingly, the lithiation plateau below 1 V indicates that  $\text{Li}^+$  could further insert into  $\omega\text{-Li}_3\text{V}_2\text{O}_5$ . As shown in Fig. 1a, DRS- $\text{Li}_3\text{V}_2\text{O}_5$  can be cycled reversibly between 0.01 V and 2 V at a current density of  $0.1\text{ A g}^{-1}$  with a specific capacity of  $266\text{ mA h g}^{-1}$ . In addition, the average working potential of 0.6 V is between those of lithium titanate and graphite, ideal for fast charging and high-energy-density applications.

To fully resolve the structure of  $\text{Li}_3\text{V}_2\text{O}_5$ , we employed joint Rietveld refinement of neutron diffraction and X-ray diffraction (XRD) patterns to quantify site occupancies in the unit cell<sup>15</sup>. The results shown in Extended Data Fig. 1c, d and Extended Data Table 1 are consistent with a DRS structure with space group  $Fm\bar{3}m$ . The cubic lattice parameter of the DRS- $\text{Li}_3\text{V}_2\text{O}_5$  is  $4.095(1)\text{ Å}$ . The O ions fully occupy the 4a sites, whereas the octahedral 4b sites are almost fully filled by Li and V ions, with 52% and 40% fractional occupancies, respectively. A few Li ions occupy 4% of the tetrahedral (8c) interstitial sites. Therefore, the structure of DRS- $\text{Li}_3\text{V}_2\text{O}_5$  can be expressed as  $[\square_{9.6}\text{Li}_{0.4}]^{8c}[\square_{0.4}\text{Li}_{2.6}\text{V}_2]^{4b}[\text{O}_5]^{4a}$ , which has plenty of vacant tetrahedral sites for hosting more Li ions.

In situ XRD was conducted while charging and discharging the electrode between 0.1 V and 2 V. The diffraction patterns (Extended Data Fig. 2c), show that the (220) peak of the rock salt phase persists throughout the entire electrochemical process. The (220) peak shifts to lower angles and broadens during Li insertion into DRS- $\text{Li}_3\text{V}_2\text{O}_5$ . The changes are completely reversible upon Li removal during charge. Similar trends were observed in neutron diffraction as shown in Fig. 1c. On the basis

<sup>1</sup>Department of Nanoengineering, University of California, San Diego, La Jolla, CA, USA. <sup>2</sup>Energy Storage and Distributed Resources Division, Lawrence Berkeley National Laboratory, Berkeley, CA, USA. <sup>3</sup>Neutron Scattering Division, Oak Ridge National Laboratory, Oak Ridge, TN, USA. <sup>4</sup>Department of Physics and Astronomy, University of California, Irvine, Irvine, CA, USA. <sup>5</sup>National Synchrotron Light Source II, Brookhaven National Laboratory, Upton, NY, USA. <sup>6</sup>Chemical Sciences and Engineering Division, Argonne National Laboratory, Argonne, IL, USA. <sup>7</sup>Center for Functional Nanomaterials, Brookhaven National Laboratory, Upton, NY, USA. <sup>8</sup>Del Norte High School, San Diego, CA, USA. <sup>9</sup>Canyon Crest Academy, San Diego, CA, USA. <sup>10</sup>Advanced Light Source Division, Lawrence Berkeley National Laboratory, Berkeley, CA, USA. <sup>11</sup>X-ray Science Division, Argonne National Laboratory, Argonne, IL, USA. <sup>12</sup>Sustainable Power and Energy Center, University of California, San Diego, La Jolla, CA, USA. <sup>13</sup>These authors contributed equally: Haodong Liu, Zhuoying Zhu. ✉e-mail: junlu@anl.gov; huolin@uci.edu; ongsp@eng.ucsd.edu; piliu@eng.ucsd.edu

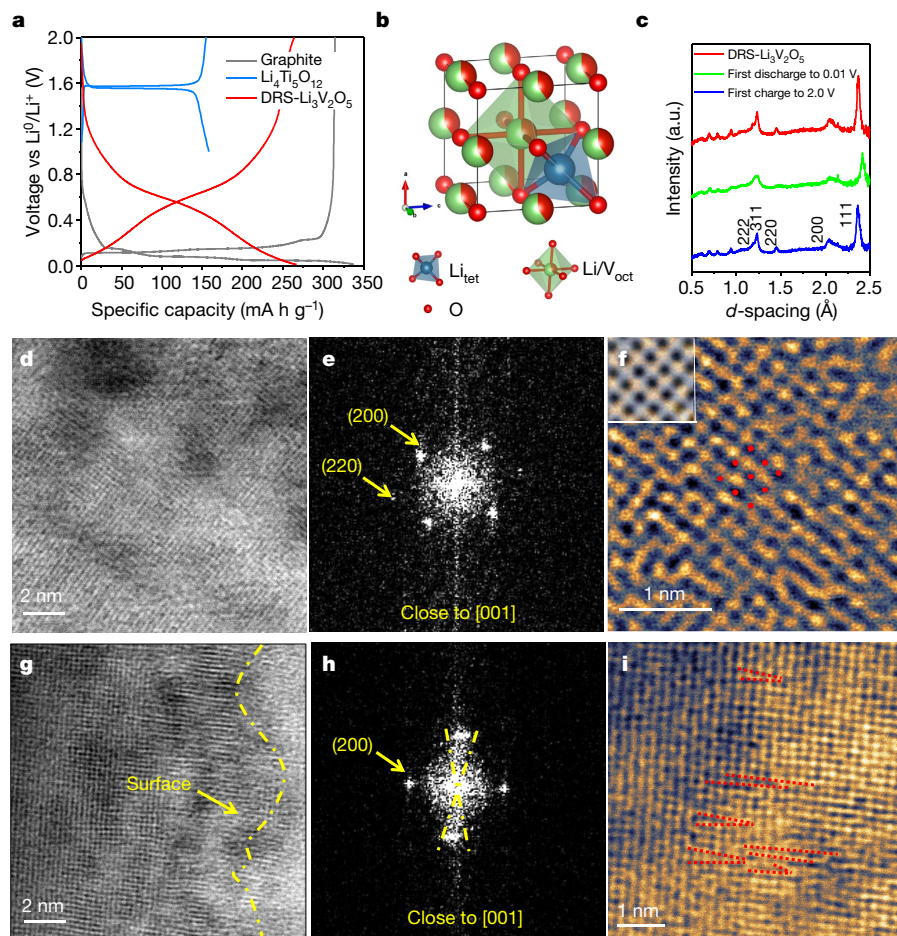


**Fig. 1 | Voltage profile and structural characterizations of the pristine and lithiated DRS- $\text{Li}_{3+x}\text{V}_2\text{O}_5$ .** **a**, The experimental voltage profiles of graphite,  $\text{Li}_4\text{Ti}_5\text{O}_{12}$  and  $\text{DRS-Li}_{3+x}\text{V}_2\text{O}_5$  under a current density of  $0.1 \text{ A g}^{-1}$ . The voltage windows for graphite,  $\text{Li}_4\text{Ti}_5\text{O}_{12}$  and  $\text{DRS-Li}_{3+x}\text{V}_2\text{O}_5$  are 0.01–2 V, 1–2 V and 0.01–2 V, respectively. **b**, The crystal structure of  $\text{DRS-Li}_3\text{V}_2\text{O}_5$ . The red balls represent O, the blue tetrahedron represents Li in tetrahedral sites, and the green octahedron represents the Li/V shared octahedral sites. **c**, Neutron diffraction patterns of  $\text{DRS-Li}_3\text{V}_2\text{O}_5$  and lithiated  $\text{DRS-Li}_{3+x}\text{V}_2\text{O}_5$ . **d–i**, Annular bright-field (ABF)-STEM images and fast Fourier transforms of  $\text{DRS-Li}_{3+x}\text{V}_2\text{O}_5$ . **d**, ABF-STEM

image of the pristine  $\text{DRS-Li}_3\text{V}_2\text{O}_5$ . **e**, The corresponding fast Fourier transform of the image in **d**, which shows face-centred cubic (fcc) structure along the [001] zone axis with relatively good crystallinity. **f**, The magnified ABF-STEM image of  $\text{DRS-Li}_3\text{V}_2\text{O}_5$ ; the inset shows a simulated ABF-STEM image of a cubic rock salt structure by a full-quantum multislice method. The simulated image shows similar patterns to the experiment that confirms the fcc structure. **g**, ABF-STEM image of the lithiated  $\text{DRS-Li}_{3+x}\text{V}_2\text{O}_5$ . **h**, The corresponding fast Fourier transform of the image in **g**. **i**, The magnified STEM image of lithiated  $\text{DRS-Li}_{3+x}\text{V}_2\text{O}_5$ , which shows some small-angle grain boundaries in the bulk.

of the (111) peak shift, the volume of the  $\text{DRS-Li}_{3+x}\text{V}_2\text{O}_5$  ( $0 \leq x \leq 2$ ) unit cell expands by only 5.9% after full lithiation, indicating that  $\text{DRS-Li}_3\text{V}_2\text{O}_5$  is highly stable as an intercalation host. The reversibility of the reaction is also confirmed by chemical analysis. The Li/V ratios of  $\text{DRS-Li}_{3+x}\text{V}_2\text{O}_5$  were measured by inductively coupled plasma optical emission spectrometry. The chemical formula of  $\text{DRS-Li}_3\text{V}_2\text{O}_5$  obtained by electrochemically lithiating  $\text{V}_2\text{O}_5$  is  $\text{Li}_{3.04}\text{V}_2\text{O}_5$ . The composition of fully lithiated  $\text{DRS-Li}_{3+x}\text{V}_2\text{O}_5$  when discharged to 0.01 V is  $\text{Li}_{4.86}\text{V}_2\text{O}_5$ , which reverts to  $\text{Li}_{2.98}\text{V}_2\text{O}_5$  when charged to 2.0 V. The inductively coupled plasma, XRD, neutron diffraction and charge/discharge results confirm that the transition between  $\text{DRS-Li}_3\text{V}_2\text{O}_5$  and  $\text{DRS-Li}_5\text{V}_2\text{O}_5$  is completely reversible.

The peak broadening of the lithiated  $\text{DRS-Li}_{3+x}\text{V}_2\text{O}_5$  in the XRD and neutron diffraction patterns, possibly induced by the local distortions inside the material, makes it difficult to quantitatively analyse the structure using the Rietveld method. We employed high-resolution scanning transmission electron microscopy (STEM) to further examine the structure. Figure 1d–f shows that the bulk of  $\text{DRS-Li}_3\text{V}_2\text{O}_5$  is well crystallized. The fast Fourier transform result shows the (200) and (220) peaks (Fig. 1e), and confirms the cubic rock salt structure. In comparison, Fig. 1g–i shows that  $\text{DRS-Li}_{3+x}\text{V}_2\text{O}_5$  maintains a rock salt structure

at 0.01 V. Small-angle grain boundaries exist in the bulk of the material, and are associated with the peak broadening observed in neutron diffraction and XRD patterns. In addition,  $\text{DRS-Li}_{3+x}\text{V}_2\text{O}_5$  is covered by an amorphous layer with a thickness of 12 nm. It is expected that a solid electrolyte interface (SEI) layer will form on the electrode surface in the operating potential region<sup>16</sup>. A statistical analysis (Extended Data Fig. 3b) shows that the thickness of the SEI ranges from 6 nm to 27 nm. The SEM images of  $\text{DRS-Li}_3\text{V}_2\text{O}_5$  in the electrode show almost no change of morphology from the  $\text{V}_2\text{O}_5$  powder (Extended Data Fig. 3c–h).

To elucidate the Li insertion mechanism in  $\text{DRS-Li}_3\text{V}_2\text{O}_5$ , density functional theory (DFT) calculations using the PBE+*U* functional were performed (see Methods for details) on different Li/V orderings in a  $\sqrt{5} \times \sqrt{5} \times 2$  supercell of the rock salt primitive cell (containing two formula units). The O anions form a face-centred cubic (fcc) sublattice with one octahedral and two tetrahedral interstitials for every O anion. Figure 2c shows the calculated site occupancies of Li ions in the octahedral and tetrahedral sites at different compositions based on the most stable DFT-relaxed structures. For the  $\text{Li}_3\text{V}_2\text{O}_5$  composition, the lowest-energy structure is one in which V and Li ions fully occupy all the octahedral sites, that is,  $[\text{Li}_3\text{V}_2]^{4b}[\text{O}_5]^{4a}$ , consistent with the structure obtained from refinement.



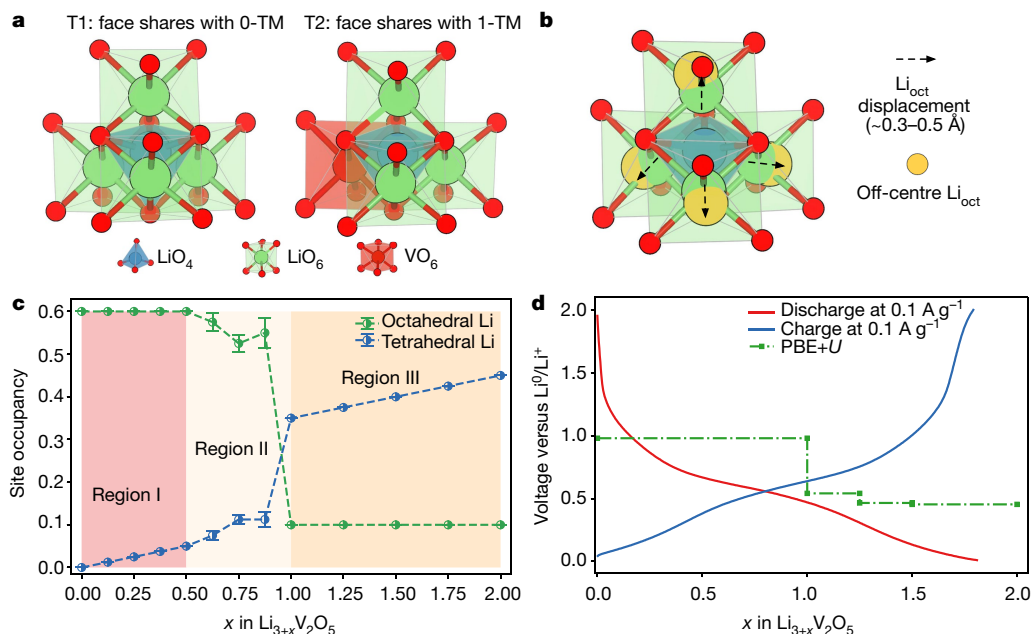


**Fig. 2 | DFT calculated Li site occupancies and voltage profile for DRS- $\text{Li}_{3+x}\text{V}_2\text{O}_5$ .** **a**, 0-TM (T1) and 1-TM (T2) tetrahedral Li insertion sites. **b**, Off-centre displacements of four neighbouring  $\text{LiO}_6$  octahedra upon Li insertion into 0-TM (T1) site. **c**, Evolution of Li site occupancies in tetrahedral and octahedral sites upon Li insertion from DFT calculations. The site

occupancies of tetrahedral and octahedral Li in all regions are calculated from three lowest-energy configurations, while the error bars are for the standard deviations of site occupancies. **d**, Experimental and computational voltage profiles calculated from the PBE+ $U$  functional.

When an Li ion is inserted into  $\text{Li}_3\text{V}_2\text{O}_5$ , it must occupy a tetrahedral site that shares faces with four occupied Li/V- $\text{O}_6$  octahedra. From the DFT-relaxed structures of  $\text{Li}_{3+x}\text{V}_2\text{O}_5$  ( $0 \leq x \leq 2$ ), we found that Li ions first preferentially insert into tetrahedral sites that share faces with four  $\text{LiO}_6$  octahedra and no  $\text{VO}_6$  octahedra, that is, 0-transition metal (0-TM) sites as shown in Fig. 2a. Insertion of Li into 1-TM sites is at least 387 meV higher in energy (see Extended Data Fig. 4a), and insertion into >1-TM sites is even more unfavourable. This is consistent with previous studies on DRS cathodes showing non-0-TM tetrahedral sites to be energetically unfavourable relative to 0-TM tetrahedral sites<sup>4</sup>. This Li insertion into a tetrahedral site is accompanied by off-centre displacements of about 0.3–0.5 Å of Li ions in the four neighbouring face-shared  $\text{LiO}_6$  octahedra to lower the overall electrostatic repulsion (see Fig. 2b). This displacement, although not negligible, is insufficient to push the Li ions from the octahedral sites into neighbouring tetrahedral sites. Hence, the initial insertion of Li is characterized by an increase in tetrahedral site occupancy with a constant Li occupancy in the octahedral sites of 0.6 as shown in Fig. 2c (region I). With further Li insertion to 0-TM tetrahedral sites, increased electrostatic repulsion results in some of the Li atoms being displaced from octahedral sites into other tetrahedral sites (region II in Fig. 2c). This region II behaviour occurs between  $x = 0.5$  and 1, and is characterized by a slightly more rapid increase in tetrahedral Li occupancy accompanied by a decrease in octahedral Li occupancy. At  $x = 1$ , we observe a redistribution of Li, resulting in a sharp decrease in the Li octahedral site occupancy to 0.1 and an increase in the Li tetrahedral site occupancy to 0.35, that is,  $[\text{Li}_{3.5}]^{8c}[\text{Li}_{0.5}\text{V}_2]^{4b}[\text{O}_5]^{4a}$ . Further insertion of Li results in a linear increase in Li tetrahedral site occupancy with the Li octahedral occupancy maintaining at 0.1 (region III in Fig. 2c). This Li redistribution mechanism is distinct from that observed in the  $\text{Li}_4\text{Ti}_5\text{O}_{12}$  (refs. <sup>17,18</sup>) and  $\text{LiMn}_2\text{O}_4$  spinels<sup>19–21</sup>, in which Li tetrahedral occupancy decreases with increasing Li octahedral occupancy.

The voltage profile of  $\text{Li}_{3+x}\text{V}_2\text{O}_5$  was determined by extracting the lowest-energy structures at each composition, computing the energies and constructing the pseudo-binary  $\text{Li}_3\text{V}_2\text{O}_5$ – $\text{Li}_5\text{V}_2\text{O}_5$  phase diagram (see Extended Data Fig. 4b). As seen in Fig. 2d, the PBE+ $U$  computed

voltage profile is in good qualitative agreement with the experimental voltage profile at the lowest current density. The initial Li insertion from  $x = 0$  to  $x = 1$  has an average PBE+ $U$  voltage of 0.98 V, followed by another voltage plateau at 0.54 V from  $x = 1$  to  $x = 1.25$ , and two final voltage plateaus at 0.46 V and 0.45 V from  $x = 1.25$  to  $x = 2$ . The overall average PBE+ $U$  voltage of 0.73 V from  $x = 0$ –2 is close to the experimental average voltage of 0.58 V. The HSE06 functional yields results similar to those from the PBE+ $U$  functional.

To investigate the charge compensation mechanism during Li-ion insertion and extraction, the normalized V K-edge X-ray absorption near edge structure (XANES) spectra are measured at different lithiation/delithiation stages, as shown in Extended Data Fig. 5a. There are two characteristic regions in the spectra: the pre-edge peaks in the range 5,465–5,470 eV, and main peaks at about 5,484 eV. The oxidation state of the V is known to be sensitive to the intensity ratio between the pre-edge and main peaks (referred to as P/M hereafter)<sup>22–24</sup>. Among the standards,  $\text{V}_2\text{O}_5$  shows the highest P/M, while  $\text{V}_2\text{O}_3$  presents the lowest P/M. It is evident that the pre-edge peak of DRS- $\text{Li}_3\text{V}_2\text{O}_5$  is between  $\text{VO}_2$  and  $\text{V}_2\text{O}_3$ , which indicates that the material predominantly consists of  $\text{V}^{4+}$  and  $\text{V}^{3+}$ . Clear changes are observed in the V K-edges after discharging to 0.01 V. The pre-edge intensity is reduced, suggesting that the oxidation state of V at 0.01 V is lower than  $\text{V}^{3+}$ . A 2-eV shift of the main peak to the lower-energy region is also observed. After the first charge, the oxidation state of V returns to between +3 and +4. The V K-edge for the material discharged to 0.01 V in the second cycle overlaps with the spectra in the first cycle, indicating that the V redox is highly reversible. On the basis of the XANES for V, we conclude that V is the only electrochemically active species. Ab initio multiple scattering calculations using the FEFF software<sup>25</sup> show a similar reduction in the P/M intensity ratio from  $\text{Li}_3\text{V}_2\text{O}_5$  to  $\text{Li}_5\text{V}_2\text{O}_5$  (Extended Data Fig. 5b) that is consistent with changes in P/M with V oxidation state for binary vanadium oxides and other lithium vanadium oxides (Extended Data Fig. 5c, d), although there are differences in the FEFF and experimental absorption edge positions.

The electrochemical cycling stability of DRS- $\text{Li}_3\text{V}_2\text{O}_5$  was evaluated first with a Li-metal counter-electrode, and then in a full cell as an anode

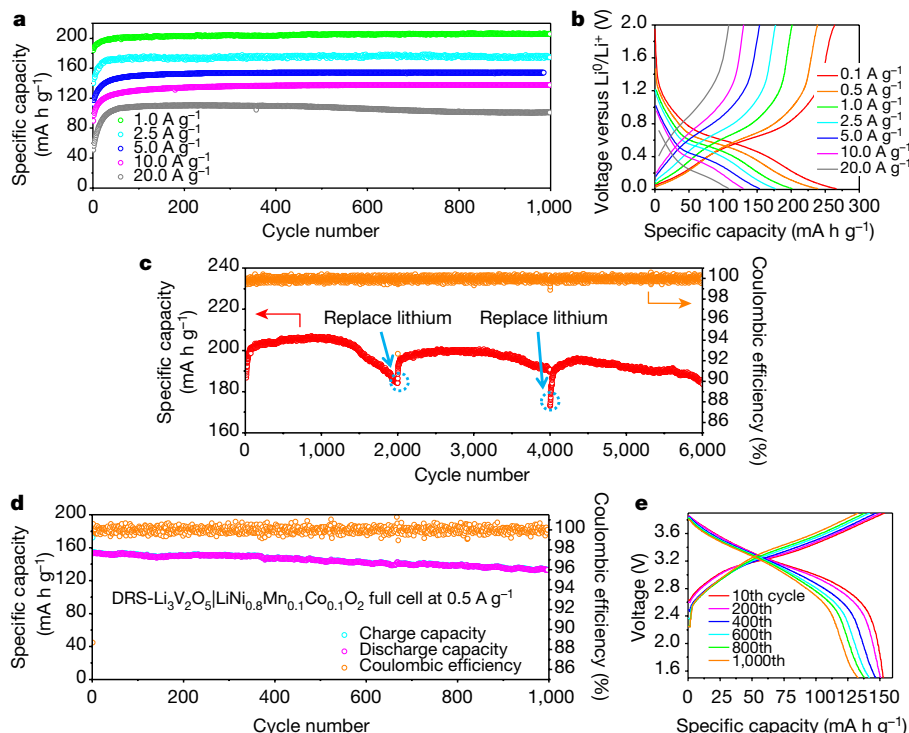


**Fig. 3 | The electrochemical performance of DRS- $\text{Li}_3\text{V}_2\text{O}_5$ .** **a**, Cycling stabilities under various charge–discharge current densities where the voltage window is 0.01–2.0 V. **b**, Voltage profiles under different current densities. **c**, Long-term stability of DRS- $\text{Li}_3\text{V}_2\text{O}_5$  at  $1 \text{ A g}^{-1}$ . **d**, The cycling stability of the DRS- $\text{Li}_3\text{V}_2\text{O}_5||\text{LiNi}_{0.8}\text{Mn}_{0.1}\text{Co}_{0.1}\text{O}_2$  full cell at  $0.5 \text{ A g}^{-1}$ . **e**, Voltage profiles over the course of 1,000 cycles for a voltage window of 1.5–3.9 V. The DRS- $\text{Li}_3\text{V}_2\text{O}_5$

electrodes with active material mass loading of  $2\text{--}3 \text{ mg cm}^{-2}$  were tested at current densities from  $0.1 \text{ A g}^{-1}$  to  $20 \text{ A g}^{-1}$ , corresponding to charge–discharge times of 2.66 h to 20 s. The DRS- $\text{Li}_3\text{V}_2\text{O}_5$  electrodes for long-term stability study were recovered from the disassembled cell and were reassembled into a coin cell with fresh electrolyte and new Li chip every 2,000 cycles.

paired with  $\text{LiNi}_{0.8}\text{Mn}_{0.1}\text{Co}_{0.1}\text{O}_2$  as the cathode. DRS- $\text{Li}_3\text{V}_2\text{O}_5$  was cycled between 0.01 V and 2 V at rates from  $0.1 \text{ A g}^{-1}$  to  $20 \text{ A g}^{-1}$  (Fig. 3a, b). Figure 3a compares the long-term stability of DRS- $\text{Li}_3\text{V}_2\text{O}_5$  at all rates. The material shows negligible capacity decay for 1,000 cycles. Its rate capability is also exceptional. As shown in Fig. 3b, at  $20 \text{ A g}^{-1}$ , the discharge capacity is  $109 \text{ mA h g}^{-1}$ , or 41% of the capacity at  $0.1 \text{ A g}^{-1}$  delivered in 20 s. Extended Data Fig. 6a shows that the charge–discharge profiles over 1,000 cycles remained virtually unchanged at a current density of  $1 \text{ A g}^{-1}$ , demonstrating its exceptional reversibility. After 1,000 cycles, the DRS- $\text{Li}_3\text{V}_2\text{O}_5$  still maintains a capacity of  $206 \text{ mA h g}^{-1}$ . In fact, we have observed 6,000 cycles of stable cycling at  $1 \text{ A g}^{-1}$  when the Li counter-electrode is periodically replaced (Fig. 3c). In addition, the stability of the DRS- $\text{Li}_3\text{V}_2\text{O}_5$  remains excellent for all cutoff voltages (Extended Data Fig. 6b, c). We note that the rate capability is demonstrated with 30% of carbon as the conducting agent in the electrode; further improvement in electronic conductivity of DRS- $\text{Li}_3\text{V}_2\text{O}_5$  through coating or doping is needed to minimize this requirement (see Methods for details).

The DRS- $\text{Li}_3\text{V}_2\text{O}_5||\text{LiNi}_{0.8}\text{Mn}_{0.1}\text{Co}_{0.1}\text{O}_2$  full cell performance was subsequently evaluated at  $0.5 \text{ A g}^{-1}$  between 1.5 V and 3.9 V (Fig. 3d, e). Here the DRS- $\text{Li}_3\text{V}_2\text{O}_5$  was prepared electrochemically from  $\text{V}_2\text{O}_5$ , although the material can be readily fabricated by chemical lithiation as well (see Methods for details). The full cell has a negative/positive electrode capacity ratio of 1.1 (Extended Data Fig. 6d). The specific capacity of the cell is  $153 \text{ mA h g}^{-1}$  (based on the  $\text{LiNi}_{0.8}\text{Mn}_{0.1}\text{Co}_{0.1}\text{O}_2$  cathode) at the first cycle with an average voltage of 3.15 V. The capacity is slightly lower than that of the  $\text{Li}||\text{LiNi}_{0.8}\text{Mn}_{0.1}\text{Co}_{0.1}\text{O}_2$  cell (Extended Data Fig. 6e, f), owing to active Li loss during cell formation cycles to form an SEI on the negative electrode surface. The capacity of the 1,000th cycle is  $133 \text{ mA h g}^{-1}$ , resulting in a capacity retention of 86.9% and an average Coulombic efficiency of  $>99.98\%$ . The charge–discharge profiles of the

cell were virtually unchanged over 1,000 cycles. The capacity decay might be due to the performance loss of the cathode caused by being cycled at high rates. The cracking and transition metal dissolution of the  $\text{LiNi}_{0.8}\text{Mn}_{0.1}\text{Co}_{0.1}\text{O}_2$  cathode were identified by scanning electron microscopy (SEM) and X-ray photoelectron spectroscopy (XPS) of the heavily cycled electrodes<sup>26–29</sup> (Extended Data Fig. 7). Overall, the stability of the DRS- $\text{Li}_3\text{V}_2\text{O}_5$  anode in Li-ion batteries is thus confirmed.

Whereas the exceptional cycling stability is likely to be a result of the small volume change, the outstanding rate performance of DRS- $\text{Li}_3\text{V}_2\text{O}_5$  can be explained by its redistributive Li insertion mechanism. Figure 4 shows the calculated nudged elastic band (NEB) barriers for Li migration at the start and end of discharge. At the start of discharge, that is,  $x \approx 0$ , we believe that Li migration takes place through a concerted mechanism whereby Li migration from the tetrahedral site to a neighbouring face-shared  $\text{LiO}_6$  octahedron is accompanied by the migration of Li in that octahedral site into another face-shared tetrahedral site. The calculated migration barriers for this mechanism are around 247–330 meV. Direct tetrahedron-to-tetrahedron hopping has much higher average barriers of about 794 meV (Extended Data Fig. 8a–c), and any hops between 0-TM and 1-TM tetrahedra have high barriers by virtue of their large site energy differences. At the end of discharge, that is,  $x \approx 2$ , most Li ions are in tetrahedral sites and about half of the octahedral sites are empty (with V octahedral occupancy at about 0.4 and Li octahedral occupancy at about 0.1). Here we considered two possible Li migration mechanisms between nearest-neighbour tetrahedral sites: direct tetrahedron-to-tetrahedron (t-t) hopping and hopping through an empty shared octahedron (t-o-t). The direct t-t mechanism has a much lower average NEB barrier of 241 meV compared to the t-o-t mechanism with an average NEB barrier of about 932 meV (see Fig. 4 and Extended Data Fig. 8d, e). The t-t mechanism has low barriers at the

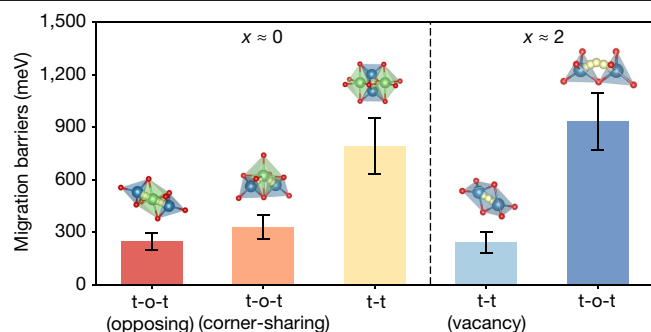


**Fig. 4 | Li migration barriers at the start of discharge ( $x \approx 0$ ) and vacancy migration barriers at end of discharge ( $x \approx 2$ ) in  $\text{Li}_{3+x}\text{V}_2\text{O}_5$ .** Calculated NEB barriers for possible Li migration hops in  $\text{Li}_3\text{V}_2\text{O}_5$  and  $\text{Li}_5\text{V}_2\text{O}_5$ . The hops are categorized in terms of their mechanism. For  $x \approx 0$ , t-o-t refers to a cooperative mechanism whereby an Li ion in a tetrahedral site hops into a neighbouring occupied octahedral site and the Li ion occupying that octahedral site hops to a neighbouring empty tetrahedron. t-t refers to a direct hop between two nearest-neighbour tetrahedra. For  $x \approx 2$ , t-o-t refers to a non-cooperative mechanism whereby an Li ion in a tetrahedral site hops through an empty octahedron to another tetrahedral site. For all mechanisms, a distribution of NEB migration barriers is shown, which is derived from 24 NEB calculations of similar mechanisms in different Li/V arrangements. The error bars represent the standard deviation of the barriers.

end of discharge, but high barriers at the start of discharge, which can be attributed to the very different octahedral occupancies. At the start of discharge, all octahedral sites are occupied, and a direct t-t hop has a transition state in which the migrating Li ions are very close to the two Li ions in the octahedral sites. Therefore, the cooperative mechanism is preferred. At the end of discharge, only half of the octahedral sites are occupied, which in turn means that about a quarter of the direct t-t hops (assuming a completely random distribution of cations) have no cations in the two neighbouring octahedra and another half have only one cation in one of the two neighbouring octahedra. The lower electrostatic repulsion in the transition state therefore results in much lower barriers. Overall, the Li migration barriers are 90–310 meV lower than those for Li migration in graphite<sup>30</sup>, which (assuming the same Arrhenius pre-factor) suggest that Li diffusion in DRS- $\text{Li}_{3+x}\text{V}_2\text{O}_5$  is more than an order of magnitude faster than in graphite. Thus, the redistributive Li insertion mechanism into DRS- $\text{Li}_{3+x}\text{V}_2\text{O}_5$  suppresses the voltage and lowers the Li migration barriers, leading to a high-energy anode with exceptional rate performance.

## Online content

Any methods, additional references, Nature Research reporting summaries, source data, extended data, supplementary information, acknowledgements, peer review information; details of author contributions and competing interests; and statements of data and code availability are available at <https://doi.org/10.1038/s41586-020-2637-6>.

- Armand, M. & Tarascon, J. M. Building better batteries. *Nature* **451**, 652–657 (2008).
- Larcher, D. & Tarascon, J. M. Towards greener and more sustainable batteries for electrical energy storage. *Nat. Chem.* **7**, 19–29 (2015).
- Grey, C. P. & Tarascon, J. M. Sustainability and in situ monitoring in battery development. *Nat. Mater.* **16**, 45–56 (2017).
- Lee, J. et al. Unlocking the potential of cation-disordered oxides for rechargeable lithium batteries. *Science* **343**, 519–522 (2014).
- Perez, A. J. et al. Approaching the limits of cationic and anionic electrochemical activity with the Li-rich layered rocksalt  $\text{Li}_3\text{IrO}_4$ . *Nat. Energy* **2**, 954–962 (2017).
- Dahn, J. R., Zheng, T., Liu, Y. & Xue, J. S. Mechanisms for lithium insertion in carbonaceous materials. *Science* **270**, 590 (1995).
- Dahn, J. R. Phase diagram of  $\text{Li}_x\text{C}_6$ . *Phys. Rev. B* **44**, 9170–9177 (1991).
- Li, H., Liu, X., Zhai, T., Li, D. & Zhou, H.  $\text{Li}_3\text{VO}_4$ : a promising insertion anode material for lithium-ion batteries. *Adv. Energy Mater.* **3**, 428–432 (2013).
- Clark, S. J., Wang, D., Armstrong, A. R. & Bruce, P. G.  $\text{Li}(\text{V}_{0.5}\text{Ti}_{0.5})\text{S}_2$  as a 1V lithium intercalation electrode. *Nat. Commun.* **7**, 10898 (2016).
- Urban, A., Matts, I., Abdellahi, A. & Ceder, G. Computational design and preparation of cation-disordered oxides for high-energy-density Li-ion batteries. *Adv. Energy Mater.* **6**, 1600488 (2016).
- Pralong, V. et al. Electrochemical synthesis of a lithium-rich rock-salt-type oxide  $\text{Li}_5\text{W}_2\text{O}_7$  with reversible deintercalation properties. *Inorg. Chem.* **53**, 522–527 (2014).
- Mikhailova, D. et al. Lithium insertion into  $\text{Li}_2\text{MoO}_4$ : reversible formation of  $(\text{Li}_3\text{Mo})\text{O}_4$  with a disordered rock-salt structure. *Chem. Mater.* **27**, 4485–4492 (2015).
- Delmas, C., Cognacouradou, H., Cocciantelli, J. M., Menetrier, M. & Doumer, J. P. The  $\text{Li}_x\text{V}_2\text{O}_5$  system—an overview of the structure modifications induced by the lithium intercalation. *Solid State Ion.* **69**, 257–264 (1994).
- Delmas, C. & Cognacouradou, H. Formation of the omega-type phase by lithium intercalation in (Mo, V) oxides deriving from  $\text{V}_2\text{O}_5$ . *J. Power Sources* **54**, 406–410 (1995).
- Yin, L. et al. Extending the limits of powder diffraction analysis: diffraction parameter space, occupancy defects, and atomic form factors. *Rev. Sci. Instrum.* **89**, 093002 (2018).
- Xu, K. Electrolytes and interphases in Li-ion batteries and beyond. *Chem. Rev.* **114**, 11503–11618 (2014).
- Aldon, L. et al. Chemical and electrochemical Li-insertion into the  $\text{Li}_4\text{Ti}_5\text{O}_{12}$  spinel. *Chem. Mater.* **16**, 5721–5725 (2004).
- Liu, H. et al. Elucidating the limit of Li insertion into the spinel  $\text{Li}_4\text{Ti}_5\text{O}_{12}$ . *ACS Mater. Lett.* **1**, 96–102 (2019).
- Thackeray, M. M., Johnson, P. J., de Picciotto, L. A., Bruce, P. G. & Goodenough, J. B. Electrochemical extraction of lithium from  $\text{LiMn}_2\text{O}_4$ . *Mater. Res. Bull.* **19**, 179–187 (1984).
- Thackeray, M. M., Mansuetto, M. F. & Bates, J. B. Structural stability of  $\text{LiMn}_2\text{O}_4$  electrodes for lithium batteries. *J. Power Sources* **68**, 153–158 (1997).
- Ramana, C. V., Massot, M. & Julien, C. M. XPS and Raman spectroscopic characterization of  $\text{LiMn}_2\text{O}_4$  spinels. *Surf. Interface Anal.* **37**, 412–416 (2005).
- Chaurand, P. et al. New methodological approach for the vanadium K-edge X-ray absorption near-edge structure interpretation: application to the speciation of vanadium in oxide phases from steel slag. *J. Phys. Chem. B* **111**, 5101–5110 (2007).
- Mansour, A. N., Smith, P. H., Baker, W. M., Balasubramanian, M. & McBreen, J. A comparative in situ X-ray absorption spectroscopy study of nanophase  $\text{V}_2\text{O}_5$  aerogel and ambigal cathodes. *J. Electrochem. Soc.* **150**, A403–A413 (2003).
- Giorgetti, M. et al. In situ X-ray absorption spectroscopy characterization of  $\text{V}_2\text{O}_5$  xerogel cathodes upon lithium intercalation. *J. Electrochem. Soc.* **146**, 2387–2392 (1999).
- Rehr, J. J., Kas, J. J., Vila, F. D., Prange, M. P. & Jorissen, K. Parameter-free calculations of X-ray spectra with FEFF9. *Phys. Chem. Chem. Phys.* **12**, 5503–5513 (2010).
- Radin, M. D. et al. Narrowing the gap between theoretical and practical capacities in Li-ion layered oxide cathode materials. *Adv. Energy Mater.* **7**, 1602888 (2017).
- Zhao, W. et al. Toward a durable solid electrolyte film on the electrodes for Li-ion batteries with high performance. *Nano Energy* **63**, 103815 (2019).
- Cheng, X. et al. Realizing superior cycling stability of Ni-rich layered cathode by combination of grain boundary engineering and surface coating. *Nano Energy* **62**, 30–37 (2019).
- Mao, Y. et al. High-voltage charging-induced strain, heterogeneity, and micro-cracks in secondary particles of a nickel-rich layered cathode material. *Adv. Funct. Mater.* **29**, 1900247 (2019).
- Thinius, S., Islam, M. M., Heitjans, P. & Bredow, T. Theoretical study of Li migration in lithium-graphite intercalation compounds with dispersion-corrected DFT methods. *J. Phys. Chem. C* **118**, 2273–2280 (2014).

**Publisher's note** Springer Nature remains neutral with regard to jurisdictional claims in published maps and institutional affiliations.

© The Author(s), under exclusive licence to Springer Nature Limited 2020



## Methods

### Preparation of electrodes

$\text{V}_2\text{O}_5$  coin cell electrodes were prepared with an active material-to-carbon-to-binder mass ratio of 6:3:1 and a diameter of 13 mm.  $\text{V}_2\text{O}_5$  powder (Sigma-Aldrich, > 99.96%) and Super P carbon black were first ground using a mortar and pestle. The powder mixture was then dispersed in a pre-mixed poly(vinylidene difluoride) (Kynar) solution in *N*-methyl pyrrolidone (Sigma-Aldrich) using a Thinky Mixer at 1,800 rpm for 2 h. The resulting slurry was cast on a copper foil (9  $\mu\text{m}$ , MTI) using a film casting doctor blade and an automatic film coater (MSK-AFA-III). Then, the film was dried under vacuum at 80 °C for 12 h. The active material loading is about 2–3  $\text{mg cm}^{-2}$ . The effect of the amount of carbon additive on the electrochemical performance of the DRS- $\text{Li}_{3+x}\text{V}_2\text{O}_5$  is presented in Extended Data Fig. 6g, h. Both electrodes contain 10 wt% of binder. At a relatively low current density of 0.1  $\text{A g}^{-1}$ , the 10 wt% (C-10) electrode delivers a specific capacity of 240  $\text{mA h g}^{-1}$ , which is slightly lower than the 30 wt% (C-30) electrode. As the current density increases to 2.5  $\text{A g}^{-1}$ , the specific capacity of the C-10 electrode drops to 93  $\text{mA h g}^{-1}$ , which is only 38.8% of its capacity at 0.1  $\text{A g}^{-1}$ . As a comparison, the specific capacity of C-30 electrode at 2.5  $\text{A g}^{-1}$  is much higher at 177  $\text{mA h g}^{-1}$ .

To prepare the  $\text{LiNi}_{0.8}\text{Mn}_{0.1}\text{Co}_{0.1}\text{O}_2$  cathode, the active material-to-carbon-to-binder mass ratio was 8:1:1, and the diameter of the electrode was 12 mm.  $\text{LiNi}_{0.8}\text{Mn}_{0.1}\text{Co}_{0.1}\text{O}_2$  (Targray) and Super C65 (TIMCAL) were directly added into a pre-mixed poly(vinylidene difluoride) solution in *N*-methyl pyrrolidone and dispersed using a Thinky Mixer at 1,800 rpm for 2 h. The slurry was then coated onto an aluminium foil (15  $\mu\text{m}$  MTI), and dried under vacuum at 120 °C for 12 h.

### Synthesis and performance evaluation of DRS- $\text{Li}_{3+x}\text{V}_2\text{O}_5$

A  $\text{V}_2\text{O}_5$  half-cell was assembled in an argon-filled glovebox with moisture and oxygen levels less than 1 ppm. For coin cells, all measurements were conducted in a stainless steel 2032 case, using a 2400 Celgard separator. An Li-metal disk (1 mm thick, 16 mm diameter) was the anode in the half-cell. The surface of the Li was cleaned with a stainless steel scalpel. The electrolyte was 1.2 M  $\text{LiPF}_6$  in 3:7 v/v ethylene carbonate (EC, BASF) and ethyl methyl carbonate (EMC, BASF) with 2 vol% vinylene carbonate (BASF). DRS- $\text{Li}_{3+x}\text{V}_2\text{O}_5$  was synthesized by electrochemically lithiating the  $\text{V}_2\text{O}_5$  to 1.5 V. The electrochemical properties of DRS- $\text{Li}_{3+x}\text{V}_2\text{O}_5$  half-cell were measured using an Arbin battery LBT-5V5A battery tester or a Land CT2001A battery tester in galvanostatic mode between 2.0 V and 0.01 V. At least five cells were electrochemically tested to confirm reproducibility.

Extended Data Fig. 6b, c shows the comparison of the electrochemical performance of DRS- $\text{Li}_3\text{V}_2\text{O}_5$  with different voltage windows under a current density of 0.1  $\text{A g}^{-1}$ . The voltage windows for DRS- $\text{Li}_3\text{V}_2\text{O}_5$  are 0.01–2 V, 0.1–2 V, 0.2–2 V and 0.3–2 V, respectively. The specific capacities of DRS- $\text{Li}_3\text{V}_2\text{O}_5$  with cut-off voltages of 0.01 V, 0.1 V, 0.2 V and 0.3 V are 260.5  $\text{mA h g}^{-1}$ , 228.7  $\text{mA h g}^{-1}$ , 198.4  $\text{mA h g}^{-1}$  and 176.4  $\text{mA h g}^{-1}$ , respectively.

The DRS- $\text{Li}_{3+x}\text{V}_2\text{O}_5$  was also paired with an  $\text{LiNi}_{0.8}\text{Mn}_{0.1}\text{Co}_{0.1}\text{O}_2$  cathode to make a full cell. The negative-to-positive electrode capacity ratio was around 1.1 (Extended Data Fig. 6d). The initial charge voltage curve of the  $\text{Li}|\text{LiNi}_{0.8}\text{Mn}_{0.1}\text{Co}_{0.1}\text{O}_2$  half-cell under 0.1  $\text{A g}^{-1}$  and the discharge voltage curve of the  $\text{Li}|\text{DRS-Li}_3\text{V}_2\text{O}_5$  half-cell under 0.1  $\text{A g}^{-1}$  were used to simulate the charge voltage profile of a DRS- $\text{Li}_3\text{V}_2\text{O}_5|\text{LiNi}_{0.8}\text{Mn}_{0.1}\text{Co}_{0.1}\text{O}_2$  full cell.  $\text{LiNi}_{0.8}\text{Mn}_{0.1}\text{Co}_{0.1}\text{O}_2$  has an initial charge specific capacity of 224  $\text{mA h g}^{-1}$  while DRS- $\text{Li}_3\text{V}_2\text{O}_5$  delivers 176  $\text{mA h g}^{-1}$  upon discharge to 0.3 V versus  $\text{Li}^+/\text{Li}$ . The voltage range of DRS- $\text{Li}_3\text{V}_2\text{O}_5$  is 0.3–2.0 V and its capacity is normalized to 1.1 times the  $\text{LiNi}_{0.8}\text{Mn}_{0.1}\text{Co}_{0.1}\text{O}_2$  capacity. The mass loading of the cathode and anode were controlled to realize a negative-to-positive electrode capacity ratio of 1.1.

### Neutron diffraction

DRS- $\text{Li}_{3+x}\text{V}_2\text{O}_5$  powders were collected at different states of (dis)charge for neutron diffraction measurement.  $\text{V}_2\text{O}_5$  electrodes prepared as

described before were punched into 58 mm  $\times$  45 mm sheets with an active loading of about 5  $\text{mg cm}^{-2}$ . Li foil pressed onto copper foil served as the counter electrode. Celgard membrane was used as the separator, and 1.2 M  $\text{LiPF}_6$  in 3:7 (volume fraction) ethyl methyl carbonate and ethylene carbonate with 2 wt% vinylene carbonate was used as the electrolyte. The pouch cell was assembled in an argon-filled glove box, and aluminium laminate was used as the case. The pouch cell was sealed under vacuum. Pouch cells were allowed to rest for 8 h to allow for adequate electrolyte wetting. LBT-5V5A battery tester (Arbin instruments) was used to (dis)charge the pouch cells to the target voltage at a specific current of 0.01  $\text{A g}^{-1}$ . To gather samples, pouch cells were disassembled in an argon-filled glove box and the DRS- $\text{Li}_{3+x}\text{V}_2\text{O}_5$  electrodes were carefully extracted. Electrodes were rinsed in dimethyl carbonate (DMC) twice for 15 s each time and allowed to dry under argon. Once dried, the electrode coating was scraped off the copper current collector using a clean surgical blade in an argon-filled glove box. The scraped-off electrode material was then rinsed in DMC three times for 15 s each time and allowed to dry under argon. Dried samples were sealed in glass vials and multiple layers of aluminium laminate before being shipped to Oak Ridge National Laboratory.

Time-of-flight neutron powder diffraction patterns were collected at the VULCAN instrument at the Spallation Neutron Source, Oak Ridge National Laboratory<sup>31</sup>. At VULCAN, approximately 0.6 g of the powder sample was loaded into a vanadium sample can of 6 mm diameter in a helium-filled glove box. An incident beam (5 mm  $\times$  12 mm) with wavelength 0.56 Å to 3.44 Å (30 Hz chopper frequency) was used, and the diffraction pattern covering the  $d$ -space 0.5–2.5 Å was collected at the  $2\theta = 90^\circ$  detector bank for a duration of 3 h. The high-intensity mode was employed with  $\Delta d/d \approx 0.45\%$ . The Spallation Neutron Source was operated at nominal 1,400-kW power. Powder neutron diffraction data were processed using VDRIVE software<sup>32</sup>. The data was normalized to the incoherent scattering pattern of a vanadium rod. Joint Rietveld refinement of the neutron and XRD data was performed using GSAS software with EXPGUI interface<sup>33,34</sup>.

### In situ XRD

The  $\text{V}_2\text{O}_5$  slurry was coated onto a Cu foil or carbon paper (Toray Carbon Paper O30) using a film casting doctor blade and an automatic film coater (MSK-AFA-III). Then, the film was dried under vacuum at 80 °C for 12 h. The coated electrode was punched into disks with diameter 14 mm, with active material loading about 5  $\text{mg cm}^{-2}$ . The AMPIX cell (Argonne's multi-purpose in situ X-ray cell), which is compatible with multiple synchrotron-based X-ray scattering and spectroscopy techniques, was employed to perform in situ XRD measurements. The in situ cell was assembled in an argon-filled glovebox with moisture and oxygen levels less than 1 ppm. There are two X-ray transmissive windows (glassy carbon) on the two sides of the AMPIX cells for achieving full penetration of XRD<sup>35</sup>. For in situ cell assembly, glass fibre (Whatman GF/D) was used as the separator and an Li-metal disk (1 mm thick, 16 mm diameter) was the anode in the cell. The electrolyte was 1.2 M  $\text{LiPF}_6$  in 3:7 v/v ethylene carbonate (BASF) and ethyl methyl carbonate (BASF). The cell was pre-cycled by discharging it to 0.1 V, then charging to 2.0 V to achieve DRS- $\text{Li}_3\text{V}_2\text{O}_5$ .

The in situ XRD data were performed at beamline 17-BM of the Advanced Photon Source at Argonne National Laboratory. A high-energy X-ray with a beam size of 0.1 mm  $\times$  0.1 mm and wavelength 0.24117 Å was used to obtain two-dimensional diffraction patterns in the transmission geometry. The cell was cycled at 0.05  $\text{A g}^{-1}$ , between 0.1 V and 2.0 V.

The X-ray penetrates the whole cell before reaching the detector for recording the diffraction pattern. All the components within the window were exposed to the X-ray, which contribute to the final diffraction pattern. It is thus important to design a cell that generates a good signal from the material, while maintaining proper electrochemical performance. The choice of the current collector is very important.

Extended Data Fig. 2a compares the XRD patterns of the in situ cell with different current collectors. Although the Cu current collector provides good electrochemical performance without contributing extra capacity, it shows too strong X-ray scattering itself. Only one (200) peak of DRS-Li<sub>3</sub>V<sub>2</sub>O<sub>5</sub> appears in the pattern, however, it overlaps with the (111) peak of Cu. As a comparison, the cell using a C paper current collector clearly shows the (111), (200) and (220) peaks of DRS-Li<sub>3</sub>V<sub>2</sub>O<sub>5</sub>. The C paper was thus chosen as the current collector for the in situ XRD experiment.

Extended Data Fig. 2b shows the voltage profile of the DRS-Li<sub>3</sub>V<sub>2</sub>O<sub>5</sub> on C paper. The C paper delivers extra capacity with some irreversible capacity loss. However, it did not impede the study of the DRS-Li<sub>3</sub>V<sub>2</sub>O<sub>5</sub>. As shown in Extended Data Fig. 2a, the (111) peak is too weak, and the (200) peak overlaps with the C paper peak. We thus conducted our analysis by focusing on the evolution of the (220) peak, which is plotted in Extended Data Fig. 2c to trace the crystal structure evolution of the DRS-Li<sub>3</sub>V<sub>2</sub>O<sub>5</sub> during the discharge and charge process. The (200) peak shifts to lower angles and broadens as Li inserts into the DRS-Li<sub>3</sub>V<sub>2</sub>O<sub>5</sub> during discharge. The reverse process happens during charging.

The lattice parameter *a* increases from 4.097(1) Å to 4.171(3) Å with Li intercalation into DRS-Li<sub>3</sub>V<sub>2</sub>O<sub>5</sub>, which corresponds to an expansion of only 1.8% (Extended Data Fig. 2d). The corresponding volume expansion is only 5.5% (Extended Data Fig. 2e). These results are consistent with ex situ neutron diffraction measurements. After delithiation, the lattice parameter *a* shrinks back to 4.101(1) Å. The asymmetric change with time during charge and discharge for the lattice parameter *a* is caused by the participation of the C paper during the charge and discharge.

### Inductively coupled plasma optical emission spectroscopy

The stoichiometry of the as-synthesized DRS-Li<sub>3+x</sub>V<sub>2</sub>O<sub>5</sub> was determined by inductively coupled plasma optical emission spectroscopy, acquired using a Perkin Elmer Optima 3000 DV.

### STEM

The atomic-resolution STEM imaging of DRS-Li<sub>3+x</sub>V<sub>2</sub>O<sub>5</sub> anode materials were performed on an FEI Talos F200X (200kV) S/TEM equipped with an X-FEG field emission source. The images were acquired in the annular bright-field (ABF) and the high-angle annular dark-field (HAADF) STEM mode. The ABF-STEM condition was formed using the lower DF2 detector. In the STEM mode, this instrument can transfer spatial information up to 1.36 Å at 200 kV, enabling atomic-resolution imaging of the DRS-Li<sub>3+x</sub>V<sub>2</sub>O<sub>5</sub> sample.

### X-ray absorption spectroscopy

The ex situ V K-edge X-ray absorption spectra were measured at beamline 5.3.1 at the Advanced Light Source, Lawrence Berkeley National Laboratory. The X-ray beam size is about 100 μm × 100 μm. The X-ray absorption spectra were collected in total fluorescence yield mode. All the X-ray absorption spectra were measured under constant helium flow in the sample chamber.

### Scanning electron microscopy

The DRS-Li<sub>3</sub>V<sub>2</sub>O<sub>5</sub> was prepared by lithiating the V<sub>2</sub>O<sub>5</sub> electrode at 0.1 A g<sup>-1</sup> until 0.01 V. The DRS-Li<sub>3+x</sub>V<sub>2</sub>O<sub>5</sub> electrodes were washed three times with DMC, then dried under vacuum for 30 min before sending to the SEM (FEI Quanta 250 SEM) stage. The samples were transferred with only 2 s exposure to the air. The V<sub>2</sub>O<sub>5</sub> powder shows irregular primary particle shapes with sizes ranging from 350 nm to 1 μm. The primary particles agglomerate into big secondary particles with sizes of tens of micrometres (Extended Data Fig. 3d, g). The V<sub>2</sub>O<sub>5</sub> and DRS-Li<sub>3</sub>V<sub>2</sub>O<sub>5</sub> in the electrode show almost no change of morphology from the V<sub>2</sub>O<sub>5</sub> powder (Extended Data Fig. 3e, h).

After 1,000 cycles, the DRS-Li<sub>3</sub>V<sub>2</sub>O<sub>5</sub>||LiNi<sub>0.8</sub>Mn<sub>0.1</sub>Co<sub>0.1</sub>O<sub>2</sub> full cell was disassembled inside an argon-filled glovebox. The LiNi<sub>0.8</sub>Mn<sub>0.1</sub>Co<sub>0.1</sub>O<sub>2</sub> electrode was washed three times with DMC, then dried under vacuum

for 30 min. SEM images of the pristine LiNi<sub>0.8</sub>Mn<sub>0.1</sub>Co<sub>0.1</sub>O<sub>2</sub> show agglomerated spherical secondary particles with diameters ranging from 6 μm to 25 μm. The surface of the pristine material is smooth, and there is no crack in the spherical particle (Extended Data Fig. 7a). The cycled LiNi<sub>0.8</sub>Mn<sub>0.1</sub>Co<sub>0.1</sub>O<sub>2</sub> exhibits different degrees of cracking on their secondary particles, from shallow cracks to a complete fracture of the 'meatball' (Extended Data Fig. 7b, c). These cracks are related to the capacity degradation of the DRS-Li<sub>3</sub>V<sub>2</sub>O<sub>5</sub>||LiNi<sub>0.8</sub>Mn<sub>0.1</sub>Co<sub>0.1</sub>O<sub>2</sub> full cell owing to poor electronic/ionic connections between particles as well as increased parasitic side reactions with the electrolyte from new surfaces<sup>26,28,29</sup>.

### XPS

The heavily cycled DRS-Li<sub>3</sub>V<sub>2</sub>O<sub>5</sub>||LiNi<sub>0.8</sub>Mn<sub>0.1</sub>Co<sub>0.1</sub>O<sub>2</sub> full cell was disassembled inside an argon-filled glovebox. The LiNi<sub>0.8</sub>Mn<sub>0.1</sub>Co<sub>0.1</sub>O<sub>2</sub> and DRS-Li<sub>3</sub>V<sub>2</sub>O<sub>5</sub> electrodes were washed three times with DMC, then dried under vacuum for 30 min before loading onto the XPS (PHI Quantera SXM) stage. The separator was directly dried under vacuum. The samples were transferred with a sealed bag made of aluminium laminate sheets (MTI) filled with argon. The samples were exposed to the argon flow during the sample loading process to avoid air contamination. XPS (PHI Quantera SXM) was carried out using an Al anode source at 15 kV and all the peaks were calibrated based on the reference C–C bond at 284.6 eV. All XPS measurements were collected using a charge neutralizer during acquisition. Survey scans were collected with a 1.0-eV step size, and were followed by high-resolution scans with a step size of 0.125 eV for the C 1s, Ni 2p, Mn 2p, Co 2p, O 1s and V 2p regions.

The separator is from the DRS-Li<sub>3</sub>V<sub>2</sub>O<sub>5</sub>||LiNi<sub>0.8</sub>Mn<sub>0.1</sub>Co<sub>0.1</sub>O<sub>2</sub> full cell after 1,000 cycles. The Ni 2p peak is clearly presented, while no signal appears in the Mn 2p and Co 2p regions (Extended Data Fig. 7d–f). Dissolution of the Ni from the cathode into the electrolyte is another well known factor resulting in the degradation of the LiNi<sub>0.8</sub>Mn<sub>0.1</sub>Co<sub>0.1</sub>O<sub>2</sub> cathode<sup>27</sup>. Extended Data Fig. 7g–j presents the XPS of the DRS-Li<sub>3</sub>V<sub>2</sub>O<sub>5</sub> from the same full cell. The O 1s spectra show only one peak of Li<sub>2</sub>CO<sub>3</sub> at around 533 eV, which is the component of the SEI in the carbonate-based electrolyte. Besides the Li<sub>2</sub>CO<sub>3</sub>, the lattice O signal at about 529 eV appears after the surface layer was removed by the Ar<sup>+</sup> etching<sup>36</sup>. At the same time, the V 2p signal was also observed at around 515 eV, indicating that the surface V contains both V<sup>3+</sup> and V<sup>4+</sup>. Similar to the separator, there is only Ni on the anode side, further confirming the dissolution of Ni from the cathode. Extended Data Fig. 7k–n presents the XPS of the LiNi<sub>0.8</sub>Mn<sub>0.1</sub>Co<sub>0.1</sub>O<sub>2</sub> from the same full cell. The surface of the cathode is similar to the DRS-Li<sub>3</sub>V<sub>2</sub>O<sub>5</sub> anode. The Ni was leached into the cathode electrolyte interface (CEI) and Li<sub>2</sub>CO<sub>3</sub> also exist in this surface layer. After Ar<sup>+</sup> etching, the Mn and Co start showing weak signals, while the peak related to the Ni oxides at about 855 eV becomes evident. This phenomenon is confirmed by the O 1s peaks, as the lattice O signal at around 529 eV also starts to dominate. The lack of V signal on the cathode side suggests that the DRS-Li<sub>3</sub>V<sub>2</sub>O<sub>5</sub> anode does not suffer from metal dissolution.

### Chemical synthesis and performance evaluation of DRS-Li<sub>3+x</sub>V<sub>2</sub>O<sub>5</sub>

Butyl-lithium was used as the lithiation reagent<sup>12,14</sup>. Stoichiometric amounts of V<sub>2</sub>O<sub>5</sub> powders were added into the 1.6 M butyl-lithium hexane solution (10% excess of butyl-lithium) with magnetic stirring for 60 min under argon atmosphere. During the reaction process, the colour of the V<sub>2</sub>O<sub>5</sub> powders changed from orange to black. The as-synthesized powders were collected by filtration and washed with hexane three times followed by drying under vacuum for 10 min at room temperature.

Extended Data Fig. 6i shows the XRD patterns of DRS-Li<sub>3</sub>V<sub>2</sub>O<sub>5</sub> prepared by different methods. The DRS-Li<sub>3</sub>V<sub>2</sub>O<sub>5</sub> synthesized by an electrochemical method is achieved by electrochemical lithiation of the V<sub>2</sub>O<sub>5</sub> in an electrochemical cell with Li metal as the counter-electrode.

# Article

The DRS-Li<sub>3</sub>V<sub>2</sub>O<sub>5</sub> synthesized by a chemical method is obtained as described above. Both XRD patterns are consistent with a cubic rock salt structure with space group  $Fm\bar{3}m$ , as indicated by the (111), (200) and (220) peaks. The chemically synthesized Li<sub>3</sub>V<sub>2</sub>O<sub>5</sub> powders were also exposed to the ambient air (22 °C, relative humidity of 50%) to investigate its stability. No change was observed in the XRD pattern after one week, indicating that the DRS-Li<sub>3</sub>V<sub>2</sub>O<sub>5</sub> anode is stable in air.

Extended Data Fig. 6j, k compares the electrochemical performance of the fresh DRS-Li<sub>3</sub>V<sub>2</sub>O<sub>5</sub> and the aged DRS-Li<sub>3</sub>V<sub>2</sub>O<sub>5</sub> prepared by chemical synthesis. Cycling stability was tested under a current density of 0.1 A g<sup>-1</sup> in the voltage window of 0.01–2 V. The specific capacity of the chemical-synthesis Li<sub>3</sub>V<sub>2</sub>O<sub>5</sub> is >200 mA h g<sup>-1</sup> at the beginning, and remains >180 mA h g<sup>-1</sup> over the course of 100 cycles. The chemically synthesized Li<sub>3</sub>V<sub>2</sub>O<sub>5</sub> has a voltage profile identical to the electrochemically synthesized Li<sub>3</sub>V<sub>2</sub>O<sub>5</sub>. The chemically synthesized Li<sub>3</sub>V<sub>2</sub>O<sub>5</sub> with air exposure for one week was also tested, and its electrochemical performance was not affected by air exposure. The prelithiation process is industrially well developed, which will greatly facilitate the scale-up of the DRS-Li<sub>3</sub>V<sub>2</sub>O<sub>5</sub> electrodes.

## DFT methods

All DFT calculations were performed using the Vienna ab initio simulation package (VASP)<sup>37</sup> with the projector augmented wave (PAW) method<sup>38</sup>. The Perdew–Burke–Ernzerhof (PBE) generalized gradient approximation (GGA) functional<sup>39</sup> with a Hubbard *U* extension (*U* value) of 3.25 eV for vanadium was adopted for structural relaxations and energy calculations<sup>40,41</sup>. All calculations were initialized in a ferromagnetic high-spin configuration because it has been previously ascertained that magnetism has a minimal impact on relative energies<sup>42</sup>. A plane wave energy cutoff of 520 eV and *k*-point density of at least 1,000 per number of atoms in the unit cell were used for initial relaxations of Li<sub>3+x</sub>V<sub>2</sub>O<sub>5</sub>, which are consistent with those massively used for the Materials Project<sup>43</sup>. The energies and forces were converged to 10<sup>-5</sup> eV per cell and 0.05 eV Å<sup>-1</sup>, respectively.

## Structure enumeration and relaxation

The candidate Li<sub>3</sub>V<sub>2</sub>O<sub>5</sub> structures were generated using  $\sqrt{5} \times \sqrt{5} \times 2$  supercells of the primitive rock salt unit cell, that is, two formula units of Li<sub>3</sub>V<sub>2</sub>O<sub>5</sub>. The occupancy of the octahedral sites (Wyckoff symbol 4b) was set at 0.6 Li:0.4 V, and all symmetrically distinct orderings generated by the enumlib<sup>44</sup> wrapper in Python Materials Genomics (pymatgen)<sup>45</sup> were fully relaxed with the PBE+*U* functional. The lowest-energy Li<sub>3</sub>V<sub>2</sub>O<sub>5</sub> ordering was then used for further analysis. Li insertion into Li<sub>3</sub>V<sub>2</sub>O<sub>5</sub> was performed by increasing the initial occupancy of the tetrahedral sites (Wyckoff symbol 8c) linearly from 0 to 0.2 (corresponding Li<sub>3</sub>V<sub>2</sub>O<sub>5</sub>) and generating all symmetrically distinct orderings and performing fully DFT structural relaxations. The orderings of the most stable Li<sub>3</sub>V<sub>2</sub>O<sub>5</sub>, Li<sub>4</sub>V<sub>2</sub>O<sub>5</sub> and Li<sub>5</sub>V<sub>2</sub>O<sub>5</sub> are given in Extended Data Fig. 9e. It was found that some Li ions in the octahedral sites automatically migrate to neighbouring tetrahedral Li sites during structural relaxations for *x* = 1, 2 in Li<sub>3+x</sub>V<sub>2</sub>O<sub>5</sub> (region III in Fig. 2c), resulting in a decrease in octahedral Li occupancy. In the Li<sub>3</sub>V<sub>2</sub>O<sub>5</sub>–Li<sub>4</sub>V<sub>2</sub>O<sub>5</sub> region, similar calculations were performed using a  $\sqrt{2} \times \sqrt{2} \times 2$  supercell of the lowest-energy Li<sub>6</sub>V<sub>4</sub>O<sub>10</sub> configuration (with formula Li<sub>24</sub>V<sub>16</sub>O<sub>40</sub>, containing 8 formula units of Li<sub>3</sub>V<sub>2</sub>O<sub>5</sub>) to obtain the *x* = 1/8, 1/4, 3/8, 1/2, 5/8, 3/4 and 7/8 structures of Li<sub>3+x</sub>V<sub>2</sub>O<sub>5</sub>. In the Li<sub>4</sub>V<sub>2</sub>O<sub>5</sub>–Li<sub>5</sub>V<sub>2</sub>O<sub>5</sub> region, calculations were performed on a  $\sqrt{2} \times \sqrt{2} \times 1$  supercell of Li<sub>6</sub>V<sub>4</sub>O<sub>10</sub> (with formula Li<sub>12</sub>V<sub>8</sub>O<sub>20</sub>) to obtain *x* = 5/4, 3/2 and 7/4 in Li<sub>3+x</sub>V<sub>2</sub>O<sub>5</sub>.

## Site occupancy calculations

The tetrahedral and octahedral Li site occupancies were calculated using the algorithm of Waroquiers et al.<sup>46</sup> When Li is initially inserted into empty tetrahedral sites in Li<sub>3</sub>V<sub>2</sub>O<sub>5</sub>, Li ions in the neighbouring face-shared octahedra are slightly displaced from the centre by approximately 0.3–0.5 Å. For the purposes of site occupancy determination,

Li ions that are determined by the algorithm to be in a 5-coordinated square pyramidal or a 6-coordinated octahedral environment are classified as being in an octahedral site, while Li ions with fourfold coordination are classified as being in a tetrahedral site. The three lowest-energy structures were used for site occupancy calculations, and the average values with error ranges are shown in Fig. 2c.

## Intercalation voltage profile

The voltage profile for Li<sub>3+x</sub>V<sub>2</sub>O<sub>5</sub> (0 ≤ *x* ≤ 2) was computed using the PBE+*U* functional<sup>47</sup>. Only the lowest-energy structure from the PBE+*U* calculations for *x* = 0, 1/8, 1/4, 3/8, 1/2, 5/8, 3/4, 7/8, 1, 5/4, 3/2, 7/4 and 2 were chosen for static calculations with a denser  $\Gamma$ -centred *k*-mesh of 5 × 5 × 5 to obtain more accurate energies. The pseudo-binary stability diagrams for Li<sub>3</sub>V<sub>2</sub>O<sub>5</sub>–Li<sub>5</sub>V<sub>2</sub>O<sub>5</sub> was then constructed and the stable intermediate phases were then used to compute the voltage profile. The average voltage between two stable intermediate phases Li<sub>*x*1</sub>V<sub>2</sub>O<sub>5</sub> and Li<sub>*x*2</sub>V<sub>2</sub>O<sub>5</sub> can be obtained from the following equation<sup>48</sup>.

$$V = - \frac{E(\text{Li}_{x_1}\text{V}_2\text{O}_5) - E(\text{Li}_{x_2}\text{V}_2\text{O}_5) - (x_1 - x_2)E(\text{Li})}{(x_1 - x_2)e}$$

where *E* is the total DFT energy and *e* is the electronic charge.

## XANES

The vanadium K-edge spectra of Li<sub>3</sub>V<sub>2</sub>O<sub>5</sub> and Li<sub>5</sub>V<sub>2</sub>O<sub>5</sub> as well as binary vanadium oxides (V<sub>2</sub>O<sub>5</sub>, VO<sub>2</sub>, V<sub>2</sub>O<sub>3</sub>) and lithium vanadium oxides (Li<sub>3</sub>VO<sub>4</sub>, LiVO<sub>2</sub>)<sup>49</sup> were calculated using the FEFF9 software library<sup>25</sup> using parameters determined in a prior high-throughput study<sup>50</sup>. The computed spectrum was shifted such that the onset absorption energy is aligned with the experimental spectrum and a Gaussian smoothing of 1 eV was applied to the computed spectrum.

## NEB calculations

NEB calculations were performed using 2 × 2 × 2 supercells of the conventional rock salt cubic unit cell. Unlike the energy and site occupancy calculations, this supercell choice was motivated by our wish to maximize the distance between periodic images of the migration path. For all NEB calculations, the initial guess for the minimum energy path is constructed with five linearly interpolated intermediate images. The energies and forces were converged to 5 × 10<sup>-5</sup> eV per supercell and 0.05 eV Å<sup>-1</sup>, respectively.

For the start of discharge, the Li:V occupancies were set at 0.59375:0.40625 such that the supercell has the formula Li<sub>19</sub>V<sub>13</sub>O<sub>32</sub>, that is, a composition of Li<sub>2.97</sub>V<sub>2.03</sub>O<sub>5</sub>, which is almost equivalent to Li<sub>3</sub>V<sub>2</sub>O<sub>5</sub>. As it is not computationally tractable to enumerate all possible Li/V orderings in such a large supercell and it is expected that only the local atomic arrangements around the migration path would have a substantial effect on the barriers, only four representative low-energy Li/V orderings (see Extended Data Fig. 9a–d) were chosen as starting structures for the NEB calculations. For each ordering, one Li ion was then inserted into a low-energy T1 (O-TM) site, and the barriers for the direct t-t and concerted t-o-t hops were calculated. For each type of hop (opposing T1-O-T1, corner-sharing T1-O-T1, edge-sharing T1-T1), the barriers for 4–7 symmetrically distinct paths were computed (see Extended Data Fig. 8a–c). As expected, the variation in barriers is relatively small for the same types of hop, justifying our use of representative configurations.

At the end of discharge, that is, *x* ≈ 2 in Li<sub>3+x</sub>V<sub>2</sub>O<sub>5</sub>, a similar 2 × 2 × 2 supercell with formula of Li<sub>32</sub>V<sub>13</sub>O<sub>32</sub> (a composition of Li<sub>5</sub>V<sub>2.03</sub>O<sub>5</sub> equivalent to Li<sub>5</sub>V<sub>2</sub>O<sub>5</sub>) was used for NEB calculations. We constructed the structure by inserting Li into O-TM and I-TM sites in the lowest-energy Li<sub>19</sub>V<sub>13</sub>O<sub>32</sub> configuration and fully relaxed it. It was found that low-energy Li/V configurations have edge-sharing LiO<sub>4</sub>-VO<sub>6</sub> to maximize the Li-V inter-cation distance and to reduce electrostatic repulsion. These low-energy structures were then used as starting structures to construct the direct tetrahedron-to-tetrahedron (t-t) hop and indirect



tetrahedron-to-octahedron-to-tetrahedron (t-o-t) hops for NEB calculations (see Extended Data Fig. 8d, e).

## Data availability

The data that support the findings of this study are available from the corresponding author on reasonable request.

31. An, K. et al. First in situ lattice strains measurements under load at VULCAN. *Metall. Mater. Trans. A* **42**, 95–99 (2011).
32. An, K., Wang, X. L. & Stoica, A. D. *Vulcan Data Reduction And Interactive Visualization Software* ORNL Report 621 (ORNL, 2012).
33. Larson, A. C. & Dreele, R. B. V. *General Structure Analysis System (GSAS)* Los Alamos National Laboratory Report (LAUR) 86-748 (LANL, 2004).
34. Toby, B. H. EXPGUI, a graphical user interface for GSAS. *J. Appl. Crystallogr.* **34**, 210–213 (2001).
35. Borkiewicz, O. J. et al. The AMPIX electrochemical cell: a versatile apparatus for in situ X-ray scattering and spectroscopic measurements. *J. Appl. Crystallogr.* **45**, 1261–1269 (2012).
36. Verde, M. G. et al. Effect of morphology and manganese valence on the voltage fade and capacity retention of  $\text{Li}[\text{Li}_{2/12}\text{Ni}_{3/12}\text{Mn}_{7/12}]\text{O}_2$ . *ACS Appl. Mater. Interfaces* **6**, 18868–18877 (2014).
37. Kresse, G. & Furthmüller, J. Efficient iterative schemes for ab initio total-energy calculations using a plane-wave basis set. *Phys. Rev. B* **54**, 11169–11186 (1996).
38. Blöchl, P. E. Projector augmented-wave method. *Phys. Rev. B* **50**, 17953–17979 (1994).
39. Perdew, J. P., Burke, K. & Ernzerhof, M. Generalized gradient approximation made simple. *Phys. Rev. Lett.* **77**, 3865–3868 (1996).
40. Padhi, A. K., Nanjundaswamy, K. S. & Goodenough, J. B. Phospho-olivines as positive-electrode materials for rechargeable lithium batteries. *J. Electrochem. Soc.* **144**, 1188–1194 (1997).
41. Liechtenstein, A. I., Anisimov, V. I. & Zaanen, J. Density-functional theory and strong-interactions—orbital ordering in Mott–Hubbard insulators. *Phys. Rev. B* **52**, R5467–R5470 (1995).
42. Ling, C., Zhang, R. G. & Mizuno, F. Phase stability and its impact on the electrochemical performance of  $\text{VOPO}_4$  and  $\text{LiVOPO}_4$ . *J. Mater. Chem. A* **2**, 12330–12339 (2014).
43. Jain, A. et al. Commentary: The Materials Project: a materials genome approach to accelerating materials innovation. *Appl. Mater.* **1**, 011002 (2013).
44. Hart, G. L. W. & Forcade, R. W. Algorithm for generating derivative structures. *Phys. Rev. B* **77**, 224115 (2008).
45. Ong, S. P. et al. Python Materials Genomics (pymatgen): a robust, open-source Python library for materials analysis. *Comput. Mater. Sci.* **68**, 314–319 (2013).
46. Waroquiers, D. et al. Statistical analysis of coordination environments in oxides. *Chem. Mater.* **29**, 8346–8360 (2017).
47. Heyd, J., Scuseria, G. E. & Ernzerhof, M. Hybrid functionals based on a screened Coulomb potential. *J. Chem. Phys.* **118**, 8207–8215 (2003).
48. Aydinol, M. K., Kohan, A. F., Ceder, G., Cho, K. & Joannopoulos, J. Ab initio study of lithium intercalation in metal oxides and metal dichalcogenides. *Phys. Rev. B* **56**, 1354–1365 (1997).
49. Rozier, P. et al. Cation-disordered  $\text{Li}_3\text{VO}_4$ : reversible Li insertion/deinsertion mechanism for quasi Li-rich layered  $\text{Li}_{1-x}[\text{V}_{1/2}\text{Li}_{1/2}]\text{O}_2$  ( $x = 0-1$ ). *Chem. Mater.* **30**, 4926–4934 (2018).
50. Zheng, C. et al. Automated generation and ensemble-learned matching of X-ray absorption spectra. *npj Comput. Mater.* **4**, 12 (2018).

**Acknowledgements** Part of the work used the UCSD-MTI Battery Fabrication Facility and the UCSD-Arbin Battery Testing Facility. Z.Z., Yiming Chen and S.P.O. acknowledge funding from the US Department of Energy (DOE), Office of Science, Basic Energy Sciences under award number DE-SC0012118 for the DFT thermodynamics and kinetic studies, the Data Infrastructure Building Blocks (DIBBS) Local Spectroscopy Data Infrastructure (LSDI) project funded by National Science Foundation (NSF), under award number 1640899 for the FEFF X-ray absorption spectroscopy computations, and computing resources provided by the Triton Shared Computing Cluster (TSCC) at the University of California, San Diego, the National Energy Research Scientific Computing Center (NERSC), and the Extreme Science and Engineering Discovery Environment (XSEDE) under grant ACI-1548562. The X-ray characterization work at Lawrence Berkeley National Laboratory by X.H. and R.K. was supported by the Assistant Secretary for Energy Efficiency and Renewable Energy, Vehicle Technologies Office, under the Advanced Battery Materials Research (BMR) Program of the U.S. Department of Energy under contract no. DE-AC02-05CH11231. Neutron diffraction work used resources at the Spallation Neutron Source, a DOE Office of Science User Facility operated by the Oak Ridge National Laboratory. R.Z. was supported by H.L.X.'s startup funding. This research used resources of the Center for Functional Nanomaterials, which is a US DOE Office of Science Facility, at Brookhaven National Laboratory under contract number DE-SC0012704. The work at Argonne National Laboratory was supported by the US DOE, Office of Energy Efficiency and Renewable Energy, Vehicle Technologies Office. This research used resources of the Advanced Photon Source (9-BM and 17-BM), Argonne National Laboratory, a US DOE Office of Science User Facility operated for the US DOE Office of Science by the University of Chicago Argonne, LLC, under contract number DE-AC02-06CH11357. M.L. would like to acknowledge financial support from the National Sciences and Engineering Research Council (NSERC) of Canada. This research thanks A. Yakovenko, W. Xu and K. Wiaderek for their support of the in situ XRD experiments. H.L. thanks J. Huang for assistance with the electrochemical experiment. H.L. and Z.Z. thank I.-H. Chu for suggestions on the DFT calculations.

**Author contributions** H.L. and P.L. conceived the ideas and designed the materials and experiments. Z.Z., Yiming Chen and S.P.O. proposed the redistributive lithium intercalation mechanism and carried out the DFT and FEFF X-ray absorption spectroscopy calculations. H.L. and Z.Z. prepared the manuscript initially. H.L., Q.Y., S.Y., X.X., Y. Choi, L.G., H.S.-y.C. and Y.L. tested the electrochemical performances and prepared all the ex situ samples. H.L., Yan Chen and K. An recorded neutron diffraction experiment data and performed data analyses. R.Z., R.L. and H.L.X. performed the TEM experiments and analyses. X.H., J.F. and R.K. conducted the ex situ X-ray absorption experiments. L.M., T.L., M.L., T.W., J.L. and K. Amine conducted the in situ XRD experiments. P.L., S.P.O., J.L. and H.L.X. supervised the research. All authors contributed to the discussion and provided feedback on the manuscript. All authors approved the final manuscript.

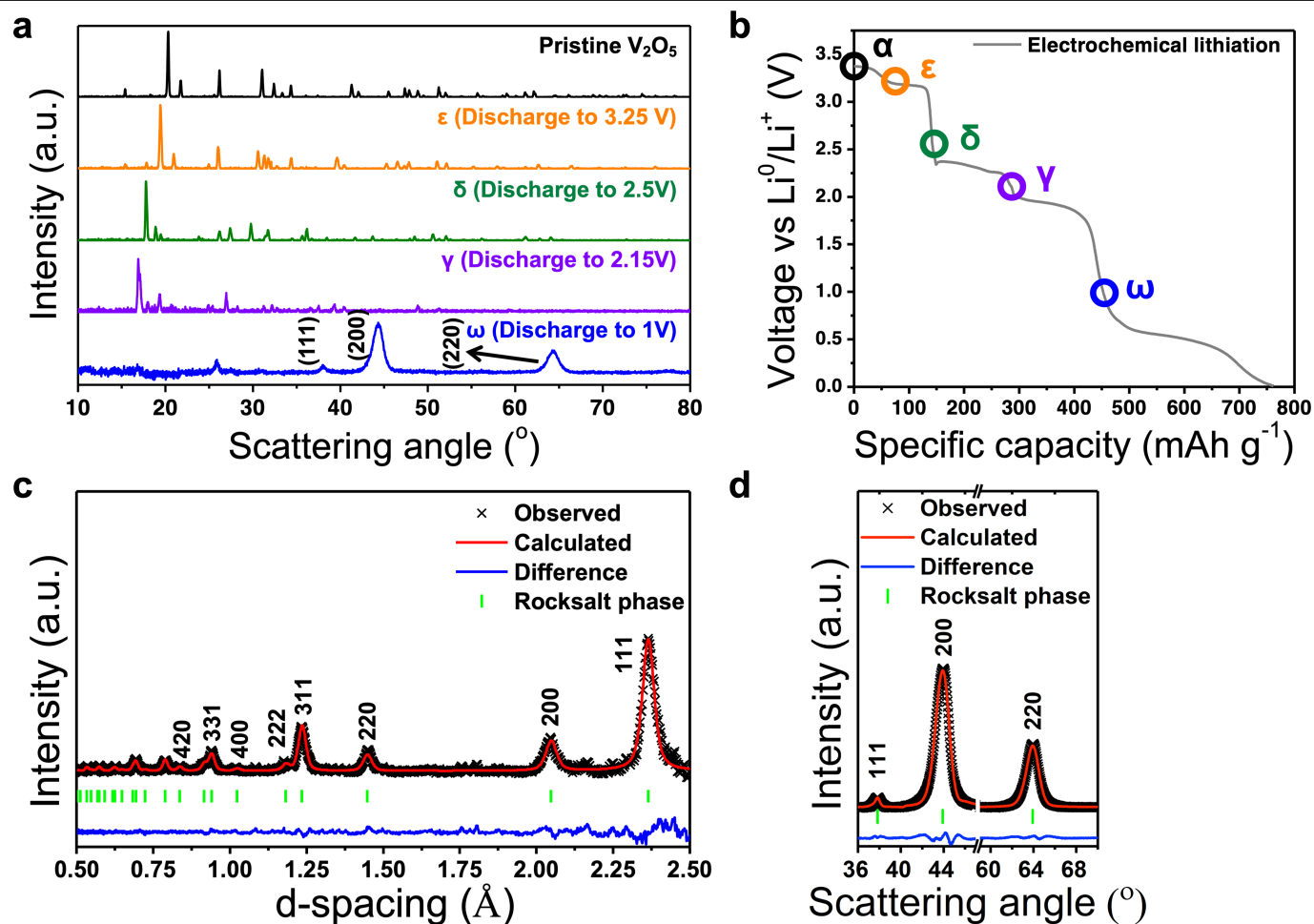
**Competing interests** P.L. and H.L. report a Patent Cooperation Treaty (PCT) application filed on 16 April 2019, Anode Material For Rechargeable Li-ion Batteries, PCT Application Serial No. US12019/27755.

### Additional information

**Supplementary information** is available for this paper at <https://doi.org/10.1038/s41586-020-2637-6>.

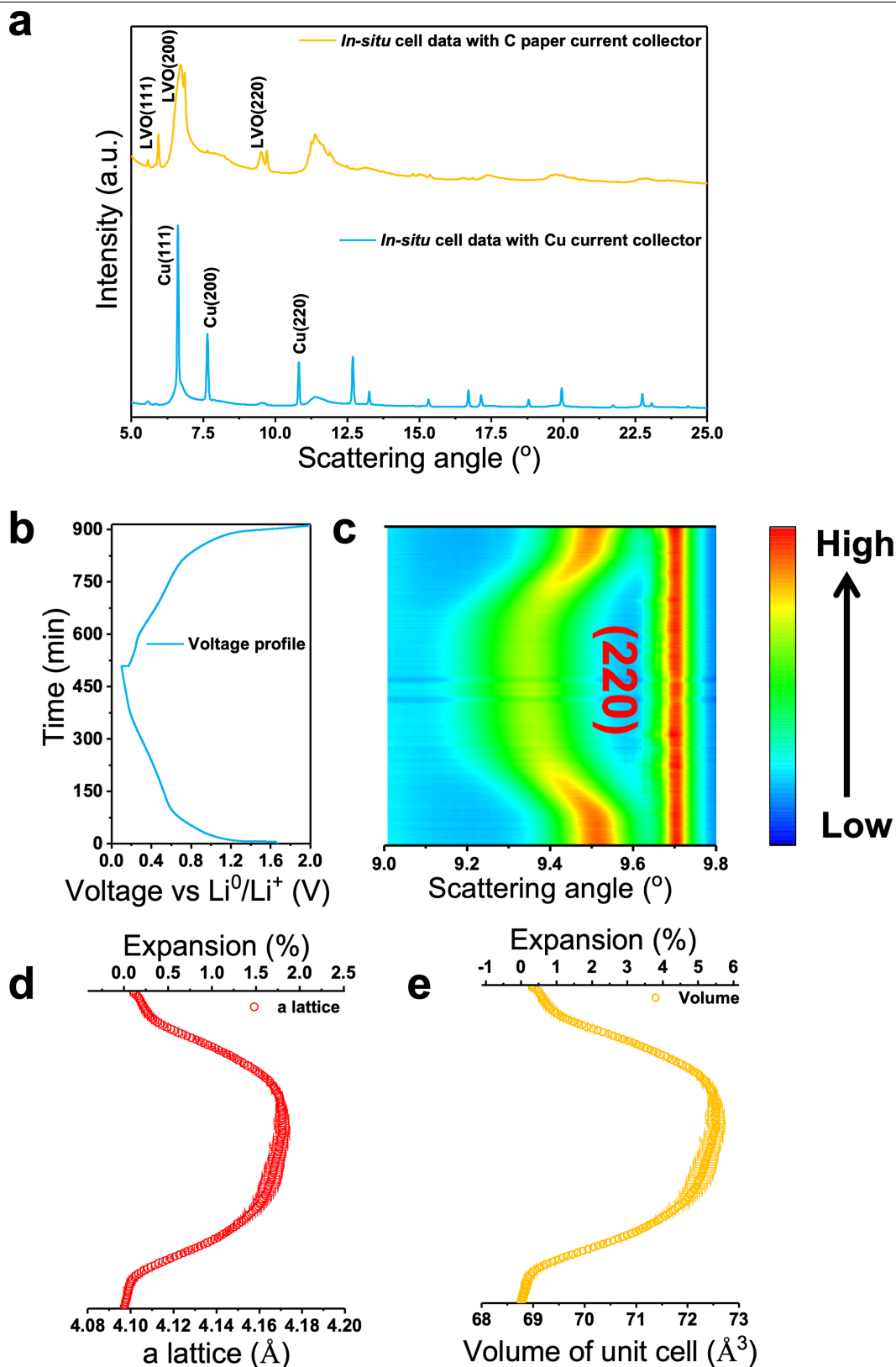
**Correspondence and requests for materials** should be addressed to J.L., H.L.X., S.P.O. or P.L. **Peer review information** *Nature* thanks Yuping Wu and the other, anonymous, reviewer(s) for their contribution to the peer review of this work.

**Reprints and permissions information** is available at <http://www.nature.com/reprints>.



**Extended Data Fig. 1 | The phase transformation process of  $\text{V}_2\text{O}_5$  upon electrochemical lithiation and joint Rietveld refinement of pristine  $\text{DRS-Li}_x\text{V}_2\text{O}_5$ .** **a**, XRD of  $\text{Li}_x\text{V}_2\text{O}_5$  ( $x=0, 0.5, 1, 2, 3$ ). The  $\text{Li}_x\text{V}_2\text{O}_5$  was obtained by electrochemical lithiation using a  $\text{Li}|\text{V}_2\text{O}_5$  cell. The cell was discharged under  $0.1 \text{ A g}^{-1}$  to 3.25 V, 2.5 V, 2.15 V and 1 V to generate the  $\epsilon$ ,  $\delta$ ,  $\gamma$  and  $\omega$  phases.

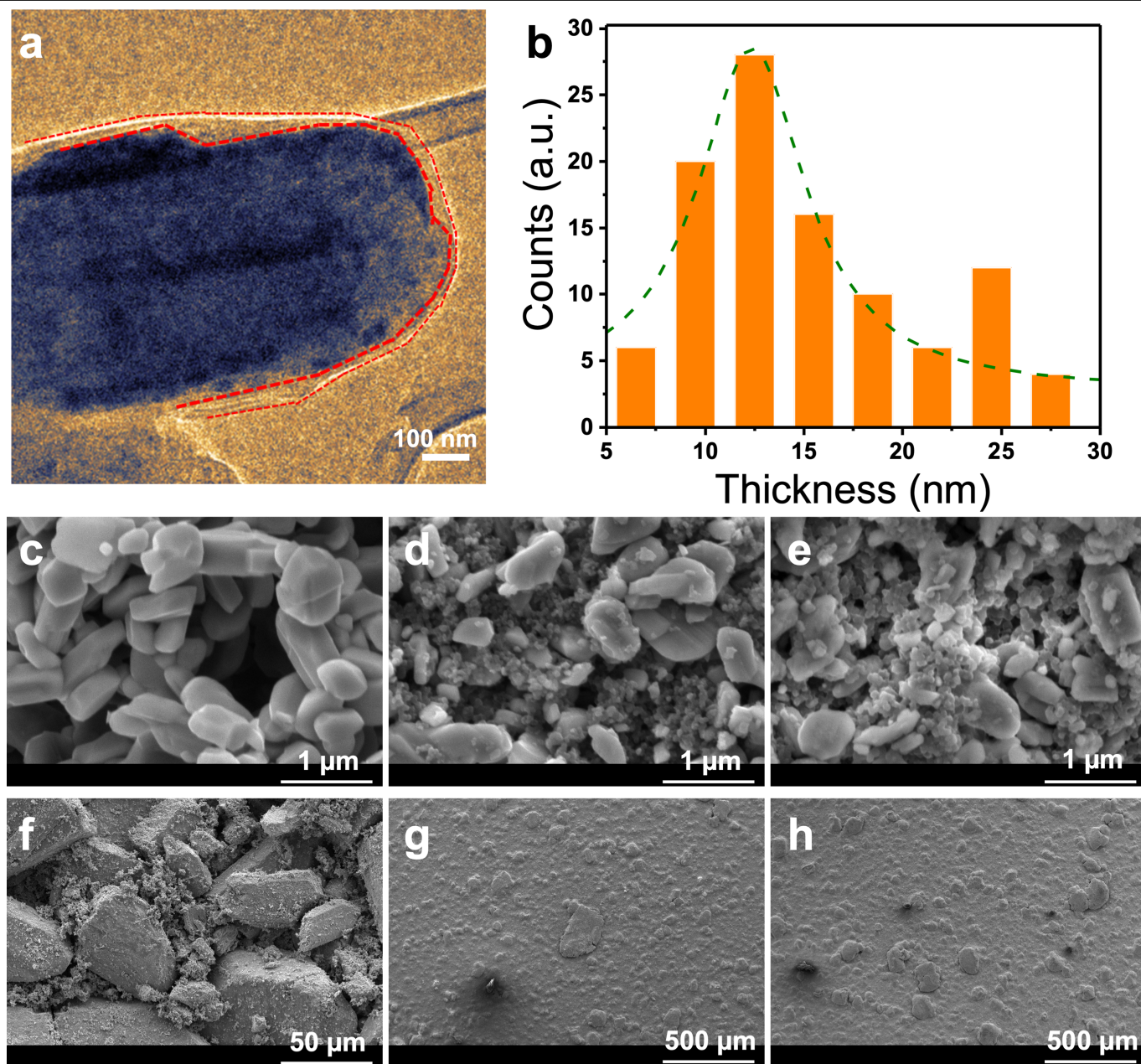
**b**, Voltage profile of the electrochemical lithiation of  $\text{V}_2\text{O}_5$  down to 0.01 V. There are five major voltage plateaus at 3.35 V, 3.18 V, 2.35 V, 1.95 V and 0.52 V, respectively. **c**, Neutron diffraction pattern; **d**, XRD pattern. The X-ray wavelength is 0.1173  $\text{\AA}$ ; the pattern is converted to the wavelength of the Cu source for comparison with the laboratory X-ray data.



**Extended Data Fig. 2 | In situ XRD study of the DRS- $\text{Li}_3\text{V}_2\text{O}_5$  during discharge and charge.** **a**, Comparison of XRD pattern of in situ cells. Carbon paper (C paper) and Cu were used as the current collectors for the DRS- $\text{Li}_3\text{V}_2\text{O}_5$  in two different AMPIX cells. The X-ray wavelength is 0.24117 Å. **b**, Voltage profile of the in situ cell with a carbon paper current collector. The DRS- $\text{Li}_3\text{V}_2\text{O}_5$

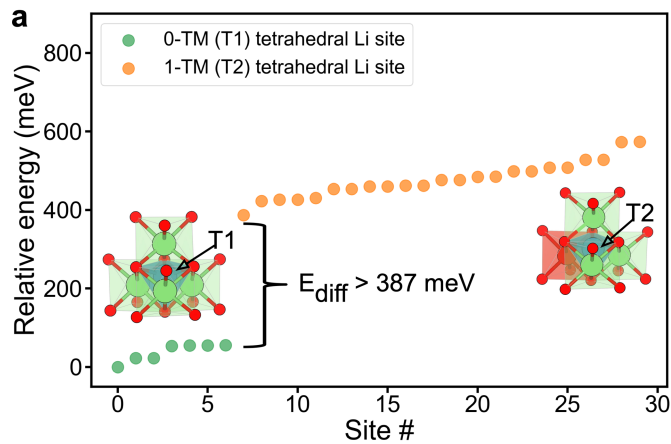
electrodes, with active material mass loading of  $5 \text{ mg cm}^{-2}$ , were cycled at a current density of  $0.05 \text{ A g}^{-1}$  between 0.1 V and 2.0 V. **c**, The corresponding contour plots of the DRS- $\text{Li}_3\text{V}_2\text{O}_5$  (220) XRD patterns. **d**, Evolution of the lattice parameter  $a$  of DRS- $\text{Li}_3\text{V}_2\text{O}_5$ . **e**, The evolution of the unit cell volume of DRS- $\text{Li}_3\text{V}_2\text{O}_5$ .



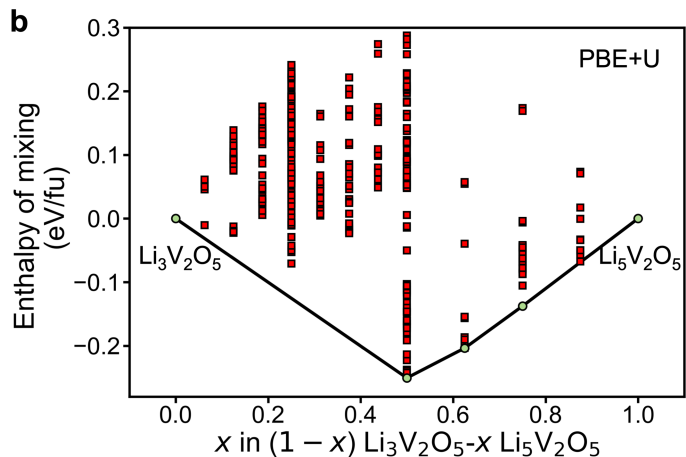


**Extended Data Fig. 3 | The characterization of the SEI layer on DRS- $\text{Li}_{3-x}\text{V}_2\text{O}_5$  and the morphologies of  $\text{V}_2\text{O}_5$  and DRS- $\text{Li}_3\text{V}_2\text{O}_5$ .** **a**, TEM images of DRS- $\text{Li}_{3-x}\text{V}_2\text{O}_5$  at 0.01 V on first discharge. The SEI layer is indicated by the red dashed lines. **b**, The statistical distribution of SEI thickness on the surface of DRS- $\text{Li}_{3-x}\text{V}_2\text{O}_5$  at 0.01 V on first discharge. (counts, the times of measurements

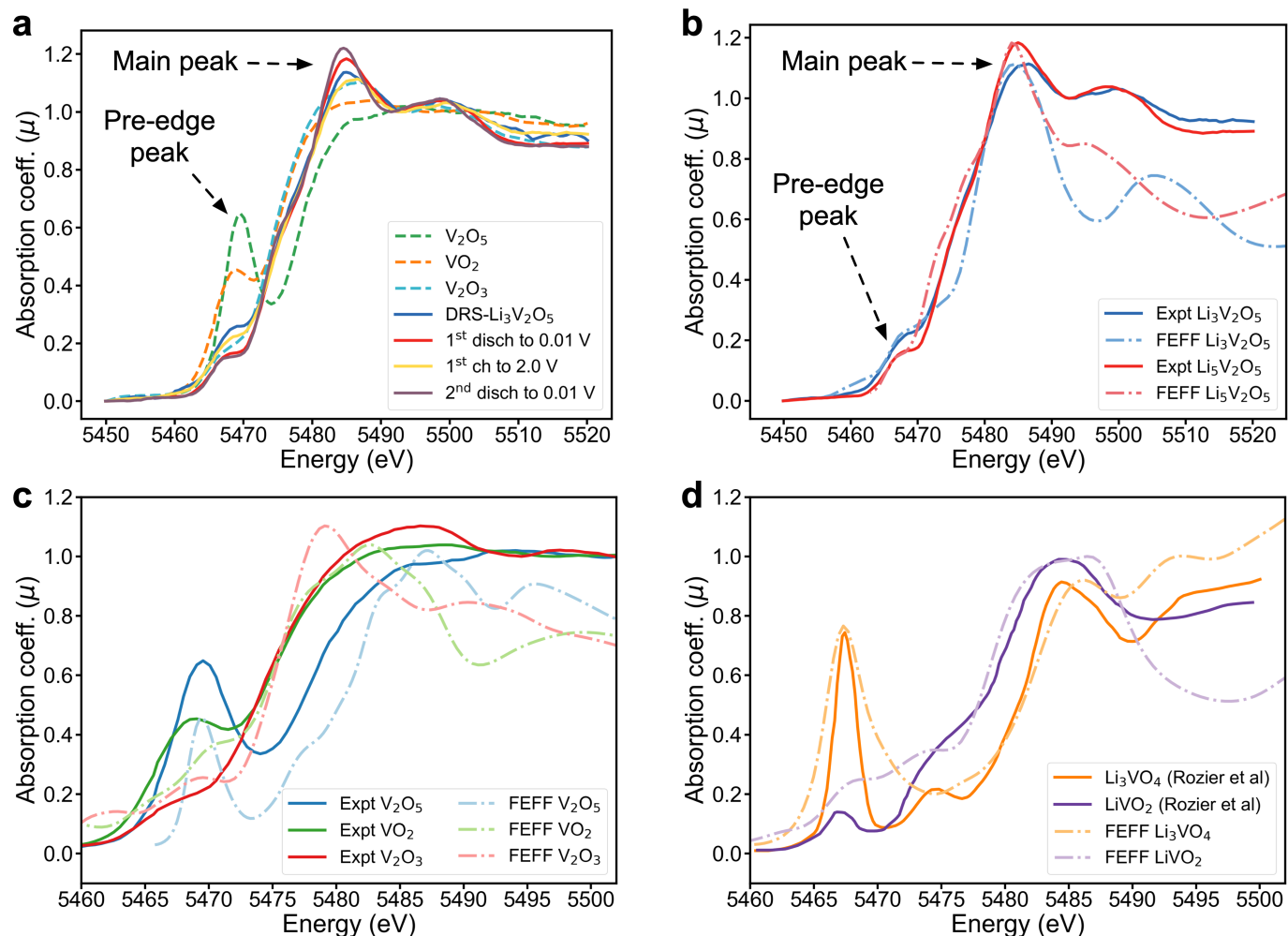
of SEI thickness; a.u., arbitrary units.) **c**, **f**, SEM images of  $\text{V}_2\text{O}_5$  powders. **d**, **g**, SEM images of the  $\text{V}_2\text{O}_5$  electrode. **e**, **h**, SEM images of DRS- $\text{Li}_3\text{V}_2\text{O}_5$ . The DRS- $\text{Li}_3\text{V}_2\text{O}_5$  was prepared by lithiating the  $\text{V}_2\text{O}_5$  electrode at  $0.1 \text{ A g}^{-1}$  until 0.01 V. The  $\text{V}_2\text{O}_5$  powder shows irregular primary particle shapes with sizes ranging from 350 nm to  $1 \mu\text{m}$ .



**Extended Data Fig. 4 | Comparison of site energies in DRS- $\text{Li}_3\text{V}_2\text{O}_5$  and pseudo-binary  $\text{Li}_3\text{V}_2\text{O}_5$ - $\text{Li}_5\text{V}_2\text{O}_5$  phase diagram from DFT calculations.** **a**, The DFT relative site energies for the 0-TM (T1) and 1-TM (T2) tetrahedral sites in  $\text{Li}_3\text{V}_2\text{O}_5$ . An additional Li ion was inserted in all symmetrically distinct sites in the lowest-energy configuration of the  $2 \times 2 \times 2$  supercell of  $\text{Li}_{10}\text{V}_{13}\text{O}_{32}$  (which is equivalent to  $\text{Li}_3\text{V}_2\text{O}_5$ ). The sites are ordered by increasing site energy, with the energy of the most stable site set as the zero reference. The seven lowest-energy sites (green circles) for Li insertion are 0-TM sites. The 1-TM sites (orange circles) have substantially higher energies ( $>387$  meV;  $E_{\text{diff}}$ , energy



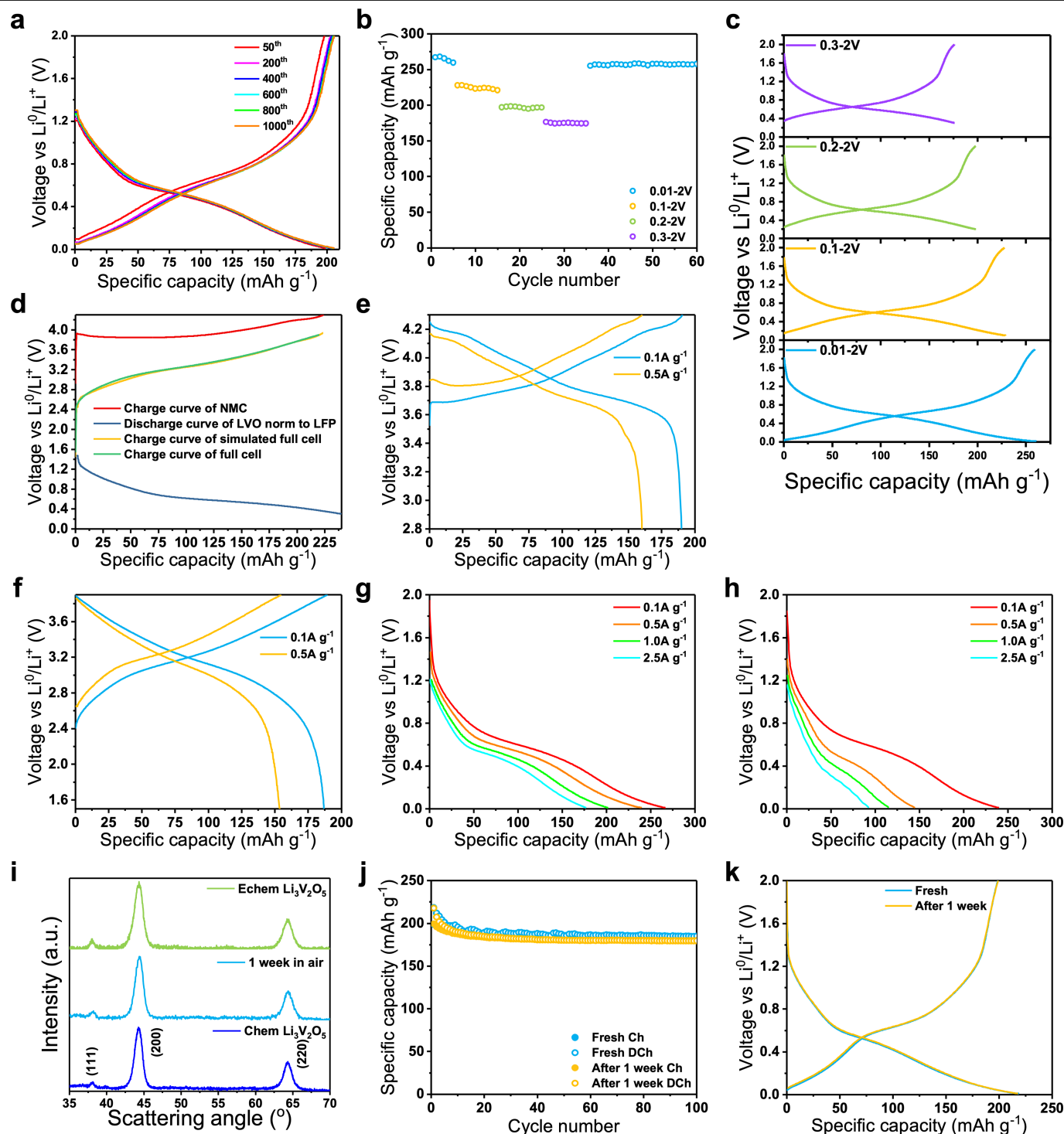
difference) for Li insertion. **b**, Pseudo-binary  $\text{Li}_3\text{V}_2\text{O}_5$ - $\text{Li}_5\text{V}_2\text{O}_5$  compound phase diagram computed using the PBE+ $U$  functional (fu, formula unit). The two endmembers are  $\text{Li}_3\text{V}_2\text{O}_5$  and  $\text{Li}_5\text{V}_2\text{O}_5$ . A finer compositional resolution of  $x = 1/8$  increments in  $\text{Li}_{3+x}\text{V}_2\text{O}_5$  was used in the  $\text{Li}_3\text{V}_2\text{O}_5$ - $\text{Li}_4\text{V}_2\text{O}_5$  region to characterize the changes in Li distribution between the tetrahedral and octahedral sites in this region. In the  $\text{Li}_4\text{V}_2\text{O}_5$ - $\text{Li}_5\text{V}_2\text{O}_5$  region, a lower compositional resolution of  $x = 1/4$  increments in  $\text{Li}_{3+x}\text{V}_2\text{O}_5$  was used because there are no changes in octahedral Li site occupancy in this region.



**Extended Data Fig. 5 | Comparison of experimental and FEFF calculated V K-edge XANES spectra reveal the charge compensation mechanism of DRS- $Li_{3+x}V_2O_5$ .** **a**, The experimental V K-edge XANES spectra at different states of (dis)charge. The dashed lines are V K-edge XANES spectra of V oxides with different V oxidation states. The oxidation states of V in  $V_2O_5$ ,  $VO_2$  and  $V_2O_3$ , are +5, +4 and +3, respectively. **b**, Comparison between experimental and FEFF-calculated V K-edge XANES spectra for  $Li_3V_2O_5$  and  $Li_5V_2O_5$ . The average oxidation states of V in  $Li_3V_2O_5$  and  $Li_5V_2O_5$  are +3.5 and +2.5, respectively.

**c**, Experimental and FEFF-calculated V K-edge XANES spectra for  $V_2O_5$ ,  $VO_2$  and  $V_2O_3$ , with V oxidation states +5, +4, +3, respectively. When V is reduced from the oxidation state of +5 to +3, the experimental V K-edge XANES spectra show a decrease in P/M. FEFF-computed V K-edge XANES spectra show the same trend. **d**, Experimental and FEFF-calculated V K-edge XANES spectra for  $Li_3VO_4$  and  $LiVO_2$ . Data are from Rozier et al.<sup>49</sup>. The average oxidation states of V in  $Li_3VO_4$  and  $LiVO_2$  are +5 and +3, respectively. A similar decrease in P/M is seen with reduction in V oxidation state.

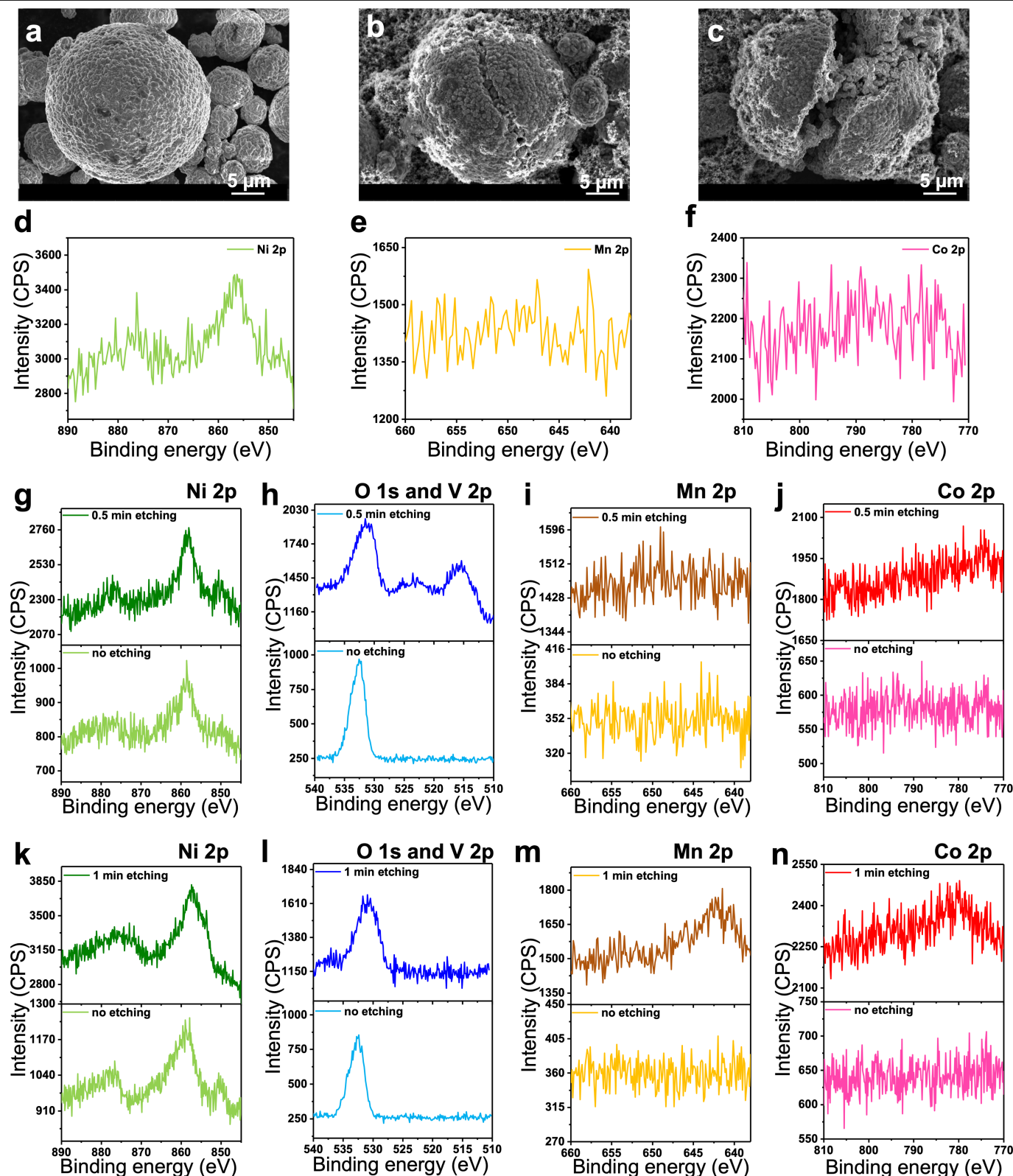




**Extended Data Fig. 6 | The electrochemical performance of DRS- $\text{Li}_3\text{V}_2\text{O}_5$ .**

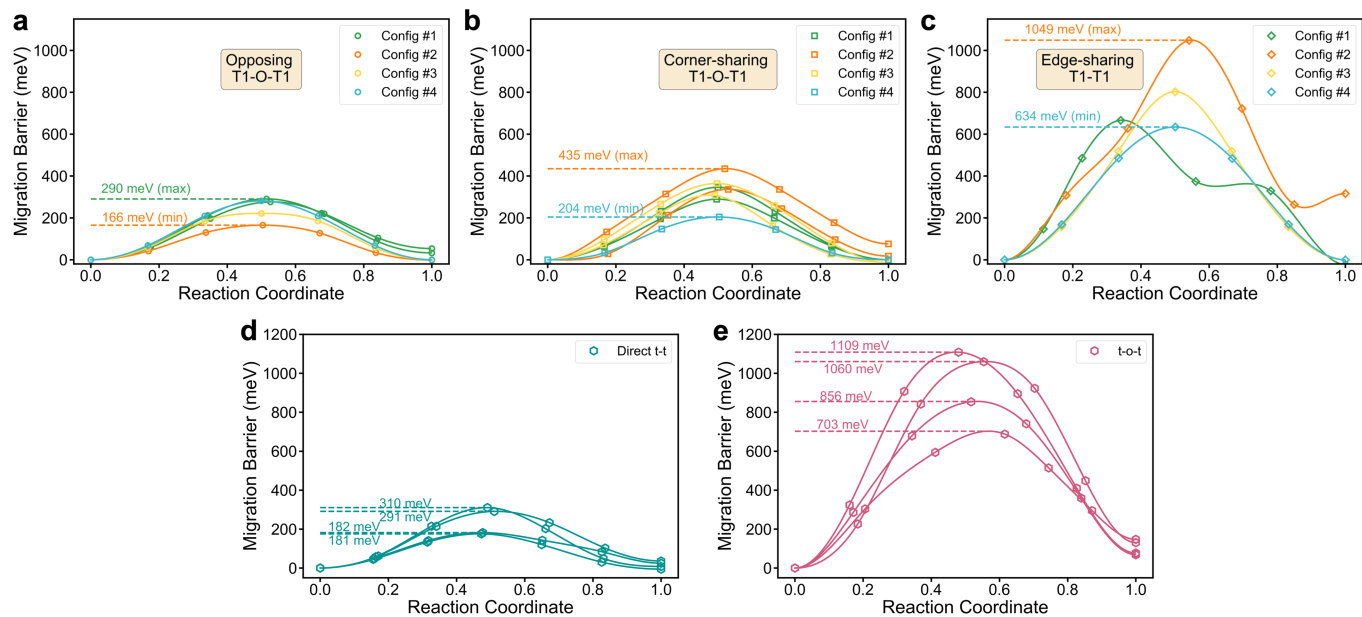
**a**, Voltage profiles of DRS- $\text{Li}_{3-x}\text{V}_2\text{O}_5$  over 1,000 cycles at  $1 \text{ A g}^{-1}$ . **b**, Comparison of the electrochemical performance of DRS- $\text{Li}_3\text{V}_2\text{O}_5$  with different voltage windows under a current density of  $0.1 \text{ A g}^{-1}$ . **c**, Voltage profiles of DRS- $\text{Li}_3\text{V}_2\text{O}_5$  in voltage windows of 0.01-2 V, 0.1-2 V, 0.2-2 V and 0.3-2 V, respectively. **d**, The initial charge voltage curve of a  $\text{Li}||\text{LiNi}_{0.8}\text{Mn}_{0.1}\text{Co}_{0.1}\text{O}_2$  half-cell under  $0.1 \text{ A g}^{-1}$  and the discharge voltage curve of a  $\text{Li}||\text{DRS-Li}_3\text{V}_2\text{O}_5$  half-cell under  $0.1 \text{ A g}^{-1}$  were used to simulate the charge voltage profile of a DRS- $\text{Li}_3\text{V}_2\text{O}_5||\text{LiNi}_{0.8}\text{Mn}_{0.1}\text{Co}_{0.1}\text{O}_2$  full cell. **e**, Voltage profiles of a  $\text{Li}||\text{LiNi}_{0.8}\text{Mn}_{0.1}\text{Co}_{0.1}\text{O}_2$  half-cell under charge-discharge current densities of  $0.1 \text{ A g}^{-1}$  and  $0.5 \text{ A g}^{-1}$ , with voltage window 2.8-4.3 V. The  $\text{LiNi}_{0.8}\text{Mn}_{0.1}\text{Co}_{0.1}\text{O}_2$  delivered specific capacities of  $190 \text{ mAh g}^{-1}$  and  $160 \text{ mAh g}^{-1}$  under  $0.1 \text{ A g}^{-1}$  and  $0.5 \text{ A g}^{-1}$ , respectively. **f**, Voltage profiles of a DRS- $\text{Li}_3\text{V}_2\text{O}_5||\text{LiNi}_{0.8}\text{Mn}_{0.1}\text{Co}_{0.1}\text{O}_2$  full cell under charge-discharge current

densities of  $0.1 \text{ A g}^{-1}$  and  $0.5 \text{ A g}^{-1}$ , with voltage window 1.5-3.9 V. The full cell delivered specific capacities of  $189 \text{ mAh g}^{-1}$  and  $155 \text{ mAh g}^{-1}$  under  $0.1 \text{ A g}^{-1}$  and  $0.5 \text{ A g}^{-1}$ , respectively. **g**, Discharge voltage profiles of DRS- $\text{Li}_3\text{V}_2\text{O}_5$  with 30 wt% of carbon under various charge-discharge current densities, with voltage window 0.01-2.0 V. **h**, Discharge voltage profiles of DRS- $\text{Li}_3\text{V}_2\text{O}_5$  with 10 wt% of carbon under various charge-discharge current densities, with voltage window 0.01-2.0 V. **i**, XRD patterns of DRS- $\text{Li}_3\text{V}_2\text{O}_5$  prepared by different methods. Comparison of the electrochemical (Echem) performance of the fresh DRS- $\text{Li}_3\text{V}_2\text{O}_5$  and the aged DRS- $\text{Li}_3\text{V}_2\text{O}_5$  prepared by chemical (Chem) synthesis. **j**, Cycling stability (Ch, charge; DCh, discharge) under a current density of  $0.1 \text{ A g}^{-1}$ . **k**, Representative voltage profiles of chemically synthesized DRS- $\text{Li}_3\text{V}_2\text{O}_5$ .



**Extended Data Fig. 7 | The failure mechanism of  $\text{LiNi}_{0.8}\text{Mn}_{0.1}\text{Co}_{0.1}\text{O}_2$  (NMC811).** **a**, SEM images of pristine  $\text{LiNi}_{0.8}\text{Mn}_{0.1}\text{Co}_{0.1}\text{O}_2$ , showing agglomerated spherical secondary particles with diameters ranging from 6  $\mu\text{m}$  to 25  $\mu\text{m}$ . **b, c**, SEM images of the  $\text{LiNi}_{0.8}\text{Mn}_{0.1}\text{Co}_{0.1}\text{O}_2$  from the DRS- $\text{Li}_3\text{V}_2\text{O}_5$ || $\text{LiNi}_{0.8}\text{Mn}_{0.1}\text{Co}_{0.1}\text{O}_2$  full cell after 1,000 cycles. The cycled  $\text{LiNi}_{0.8}\text{Mn}_{0.1}\text{Co}_{0.1}\text{O}_2$  exhibits different degrees of cracking on their secondary particles. **d-f**, XPS of the separator from the cycled DRS- $\text{Li}_3\text{V}_2\text{O}_5$ || $\text{LiNi}_{0.8}\text{Mn}_{0.1}\text{Co}_{0.1}\text{O}_2$  full cell: **d**, Ni 2p region; **e**, Mn 2p region; **f**, Co 2p region. The separator is from the DRS- $\text{Li}_3\text{V}_2\text{O}_5$ || $\text{LiNi}_{0.8}\text{Mn}_{0.1}\text{Co}_{0.1}\text{O}_2$  full cell after 1,000 cycles. The Ni 2p peak is clearly presented, while no signal appears in the

Mn 2p and Co 2p regions. (CPS, counts per second.) **g-j**, XPS of the DRS- $\text{Li}_3\text{V}_2\text{O}_5$  electrode from the same full cell before and after etching: **g**, Ni 2p region; **h**, O 1s and V 2p region; **i**, Mn 2p region; **j**, Co 2p region. Similar to the separator, there is only Ni on the anode side, further confirming the dissolution of Ni from the cathode. **k-n**, XPS of the  $\text{LiNi}_{0.8}\text{Mn}_{0.1}\text{Co}_{0.1}\text{O}_2$  electrode from the same full cell: **k**, Ni 2p region; **l**, O 1s and V 2p region; **m**, Mn 2p region; **n**, Co 2p region. The lack of V signal on the cathode side suggests that the DRS- $\text{Li}_3\text{V}_2\text{O}_5$  anode does not suffer from metal dissolution.



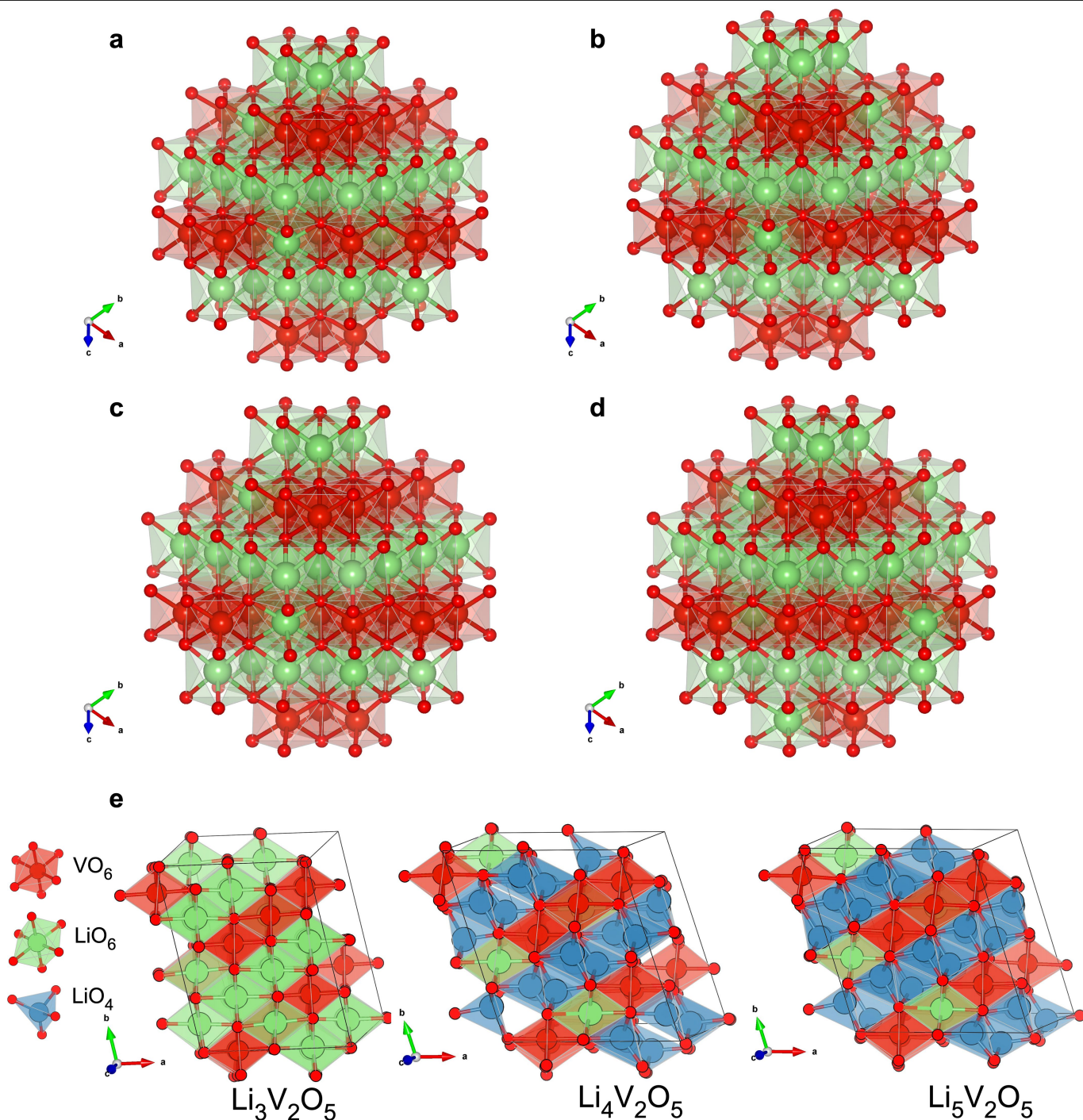
**Extended Data Fig. 8 | NEB barriers categorized by their mechanism at the start ( $x \approx 0$ ) and end ( $x \approx 2$ ) of the discharge in  $\text{Li}_{3-x}\text{V}_2\text{O}_5$ .** Panels **a–c** refer to Li interstitial migration barriers in  $\text{Li}_{19}\text{V}_{13}\text{O}_{32}$  (equivalent to  $\text{Li}_3\text{V}_2\text{O}_5$ ) and panels **d** and **e** refer to Li vacancy migration in  $\text{Li}_{32}\text{V}_{13}\text{O}_{32}$  (equivalent to  $\text{Li}_5\text{V}_2\text{O}_5$ ).

**a**, Concerted Li migration barriers in  $\text{Li}_3\text{V}_2\text{O}_5$  based on four representative configurations. Five paths from four orderings contribute to super-low NEB barriers ranging from 166 meV to 290 meV. The hopping type is opposing T1-O-T1, which refers to cooperative hops between two T1 (O-TM) tetrahedral sites through an octahedral site. The relative positions between the initial and final tetrahedral sites are opposing versus the central octahedral site.

**b**, Concerted Li migration barriers in  $\text{Li}_3\text{V}_2\text{O}_5$  based on four representative configurations. Seven paths from four orderings contribute to relatively low NEB barriers ranging from 204 meV to 435 meV. The hopping type is corner-sharing T1-O-T1, which refers to cooperative hops between two T1

(O-TM) tetrahedral sites through an octahedral site. The relative positions between the initial and final tetrahedral sites are corner-shared with each other. **c**, Direct Li migration barriers in  $\text{Li}_3\text{V}_2\text{O}_5$  based on four representative configurations. Four paths from four orderings contribute to high NEB barriers ranging from 634 meV to 1,049 meV. The hopping type is edge-sharing T1-T1, which refers to the direct hops between two nearest edge-sharing T1 (O-TM) tetrahedral sites. **d**, Vacancy migration barriers in the lowest-energy configuration of  $\text{Li}_5\text{V}_2\text{O}_5$ . Direct tetrahedron-to-tetrahedron (t-t) hops with super-low NEB barriers ranging from 181 meV to 310 meV. **e**, Hops by the t-o-t mechanism refer to the migration from one tetrahedron to the other through an empty face-shared octahedron. The barriers from 703 meV to 1,109 meV are much higher than for the direct t-t mechanism, which makes this mechanism unfavourable.





**Extended Data Fig. 9 | Four representative configurations of  $\text{Li}_9\text{V}_{13}\text{O}_{32}$  (equivalent to  $\text{Li}_3\text{V}_2\text{O}_5$ ) with low energies and the most stable ordered structures of  $\text{Li}_{3-x}\text{V}_2\text{O}_5$  ( $x = 0, 1, 2$ ) after structure enumeration.** The configurations **a** to **d** are obtained from  $2 \times 2 \times 2$  supercells of the rock salt cubic conventional cell. Octahedral sites are fully occupied by Li/V atoms (green octahedra are  $\text{LiO}_6$ , red octahedra are  $\text{VO}_6$ ). These representative configurations were used for NEB calculations at the start of discharge.

**e**,  $\text{LiO}_4$  tetrahedra and  $\text{LiO}_6$  octahedra are shown as blue and green polyhedral, respectively, when red ones are for  $\text{VO}_6$  octahedra. From the structure of  $\text{Li}_3\text{V}_2\text{O}_5$  to  $\text{Li}_4\text{V}_2\text{O}_5$ , the majority of octahedral Li transfer to tetrahedral Li, which is consistent with site occupancy results in Fig. 2c. When Li continues to be inserted, the number of  $\text{LiO}_6$  octahedra remain the same and  $\text{LiO}_4$  tetrahedra keep increasing.



Extended Data Table 1 | Results of joint refinement of X-ray and neutron diffraction of DRS-Li<sub>3</sub>V<sub>2</sub>O<sub>5</sub> powders

DRS-Li <sub>3</sub> V <sub>2</sub> O <sub>5</sub> , Space Group: Fm $\bar{3}$ m					
a=b=c 4.095(1) Å,					
Neutron pattern: R <sub>wp</sub> = 2.76%					
X-ray pattern: R <sub>wp</sub> = 2.37%					
<i>Atom type</i>	<i>WyckSymb</i>	<i>x</i>	<i>y</i>	<i>z</i>	<i>Occupancy</i>
Li	4b	0	0	0.5	0.52(1)
V	4b	0	0	0.5	0.4
O	4a	0	0	0	1
Li	8c	0.25	0.25	0.25	0.04(1)

Rwp: weighted profile R-factor. WyckSymb, Wyckoff Symbol, a notation to represent Wyckoff position in crystallography.